The *JWST* EXCELS survey: direct estimates of C, N, and O abundances in two relatively metal-rich galaxies at $z \simeq 5$

K. Z. Arellano-Córdova [1]⋆ F. Cullen [1] A. C. Carnall [1] D. Scholte [1] T. M. Stanton [1]
C. Kobayashi [2] Z. Martinez [3] D. A. Berg [3] L. Barrufet [1] R. Begley [1] C. T. Donnan [1]
J. S. Dunlop,[1] M. L. Hamadouche [4] D. J. McLeod [1] R. J. McLure,[1] K. Rowlands [5,6]
and A. E. Shapley[7]

[1]*Institute for Astronomy, University of Edinburgh, Royal Observatory, Edinburgh EH9 3HJ, UK*
[2]*Centre for Astrophysics Research, Department of Physics, Astronomy and Mathematics, University of Hertfordshire, Hatfield AL10 9AB, UK*
[3]*Department of Astronomy, The University of Texas at Austin, 2515 Speedway, Stop C1400, Austin, TX 78712, USA*
[4]*Department of Astronomy, University of Massachusetts, Amherst, MA 01003, USA*
[5]*AURA for ESA, Space Telescope Science Institute, 3700 San Martin Dr, Baltimore, MD 21218, USA*
[6]*William H. Miller III Department of Physics and Astronomy, Johns Hopkins University, Baltimore, MD 21218, USA*
[7]*Department of Physics & Astronomy, University of California, 430 Portola Plaza, Los Angeles, CA 90095, USA*

ABSTRACT

We present a spectroscopic analysis of two star-forming galaxies at $z \simeq 5$ observed with *JWST*/NIRSpec as part of the Early eXtragalactic Continuum and Emission Line Science survey. The detection of the C III] $\lambda\lambda$1906,09, [O II] $\lambda\lambda$3726,29, [O III] $\lambda\lambda$4363,5007, and [N II] λ6584 emission lines enables an investigation of the C/O, N/O, and C/N abundance ratios using the temperature-sensitive method. The galaxies have stellar masses of $\log(M_\star/M_\odot) = 8.09^{+0.24}_{-0.15}$ and $\log(M_\star/M_\odot) = 8.02^{+0.06}_{-0.08}$ with metallicities of $Z \simeq 0.2\,Z_\odot$ and $Z \simeq 0.3\,Z_\odot$. These metallicities are somewhat higher than is typical for other $z \gtrsim 5$ galaxies with similar stellar mass and are comparable to $z \simeq 0$ analogues. Both galaxies display evidence for elevated N/O ratios with respect to the typical star-forming galaxies at $z \simeq 0$, with $\log(N/O) = -1.07^{+0.17}_{-0.13}$ and $\log(N/O) = -0.86^{+0.15}_{-0.11}$, respectively. In contrast, we find low C abundances, with $\log(C/O) = -0.82 \pm 0.22$ and $\log(C/O) = -1.02 \pm 0.22$, consistent with the predicted yields of core-collapse supernovae. Following the trend observed in other high-redshift sources, we find that the C/N ratios are lower at fixed O/H compared to the majority of local galaxies. Via a comparison to detailed chemical evolution models, we find that a standard or bottom-heavy initial mass function can explain the observed abundance ratios where the N-enrichment comes from intermediate-mass ($\simeq 4$–$7\,M_\odot$) stars. Our results demonstrate that robust measurements of CNO abundances with *JWST* can reveal unique enrichment pathways in galaxies as a function of both metallicity and redshift.

Key words: ISM: abundances – H II regions – Galaxy: abundances – Galaxy: disc – Galaxy: evolution.

1 INTRODUCTION

Carbon (C), nitrogen (N), and oxygen (O) are important tracers of the chemical enrichment of the interstellar medium (ISM) in star-forming regions. Since these elements are formed on different time-scales, the relative abundances of C and N in relation to O (i.e. C/O and N/O) are crucial for tracing the star formation history and chemical evolution of galaxies.

Nitrogen is produced in both massive stars ($> 10\,M_\odot$) and intermediate-mass stars ($\simeq 4$–$7\,M_\odot$). At high metallicity, the majority of N production arises from intermediate-mass stars during the asymptotic giant branch (AGB) phase, while at low metallicities, massive stars eject N stellar winds on short time-scales ($\sim$25 Myr) (e.g. Henry, Edmunds & Köppen 2000; Kobayashi, Karakas & Umeda 2011; Vincenzo et al. 2016; Kobayashi, Karakas & Lugaro

2020). Carbon is created in triple-α reactions within massive stars and also within low-mass AGB stars ($\simeq 1$–$4\,M_\odot$). The ejection of oxygen (and most other α-elements) occurs at core-collapse supernovae (CCSNe) of massive stars (on $\sim$40 Myr time-scale) (e.g. Kobayashi et al. 2020; Arellano-Córdova et al. 2024). Oxygen is used as a proxy of the total metallicity of the ISM, and is typically parametrized with the number ratios as 12+log(O/H).

While oxygen and nitrogen abundances can be analysed via the rest-frame optical spectra of photoionized objects (e.g. Pérez-Montero & Contini 2009; Croxall et al. 2016; Berg et al. 2019b, 2016, 2021; Arellano-Córdova & Rodríguez 2020; Izotov et al. 2023), the faintness of the optical C II λ4267 recombination lines makes them extremely difficult to detect across a wide range of physical conditions (e.g. Esteban et al. 2005; Skillman et al. 2020). However, the C III] λ1906 and [C III] λ1909[1] collisionally excited

⋆ E-mail: ziboney@gmail.com, k.arellano@ed.ac.uk

[1]We represent the C III] and [C III] lines as C III] $\lambda\lambda$1906,09 in this work.

lines (CELs) are among the brightest features in the ultraviolet (UV) regime, enabling analyses of the C/O ratio in galaxies across a wide range of redshifts (e.g. Garnett 1990; Berg et al. 2016, 2019b; Peña-Guerrero et al. 2017; Arellano-Córdova et al. 2022).

Observations with the *JWST* have recently provided crucial information on additional ionization states of N that can be observed in the rest-frame UV, facilitating studies of N enrichment in the very early Universe (Bunker et al. 2023). The N IV] $\lambda\lambda1483,86$ and N III] $\lambda\lambda1750-54$ UV lines are now frequently used to derive the N/O in objects at $z \gtrsim 6$ (Cameron et al. 2023; Isobe et al. 2023b; Marques-Chaves et al. 2023; Curti et al. 2025; Ji et al. 2024; Schaerer et al. 2024; Topping et al. 2025, b). Interestingly, chemical abundance studies using the UV N lines have revealed extremely high N/O enrichment in some early sources (e.g. GN-z11 at $z = 10.6$; Bunker et al. 2023; Cameron et al. 2023). Such high N/O ratios are puzzling, since the nucleosynthesis of N and O are expected to follow similar pathways at low metallicity (e.g. Berg et al. 2016, 2019a; Vincenzo et al. 2016).

Several scenarios have been proposed to explain these elevated N abundance in star-forming galaxies (SFGs) at the highest redshifts. Possible explanations include winds from very massive stars ($\gtrsim 100\,M_{\odot}$; Vink 2023) and/or supermassive stars ($\simeq 10^4\,M_{\odot}$; Charbonnel et al. 2023; Watanabe et al. 2024), precursors of globular clusters (e.g. Senchyna et al. 2024), the presence of active galactic nuclei (AGNs; Maiolino et al. 2024), or shocks and Wolf–Rayet (WR) stars (Flury et al. 2024). Additionally, Kobayashi & Ferrara (2024) used chemical evolution models to reproduce the C/O and N/O abundance ratios of GN-z11, concluding that galaxies with two bursts of star formation followed by a quiescent phase of $\simeq 100$ Myr can successfully reproduce the observed abundance patterns. Kobayashi & Ferrara (2024) suggest that the quiescent phase can be related to outflows, while the first burst of star formation can be triggered by pre-enriched gas from external galaxies.

Although most recent high-redshift N abundance determinations have been derived mainly with UV N lines, studies of SFGs at intermediate redshifts ($z \simeq 2 - 3$) have used the optical [N II] $\lambda6584$ line (Sanders et al. 2023a; Rogers et al. 2024; Welch et al. 2025). These studies also typically return a high value of N/O in comparison with local SFGs, albeit less extreme than for the $z > 6$ sources. The reason for these elevated N/O ratios has been attributed to pristine gas inflows that can dilute the metallicity at fixed N/O (Amorín, Pérez-Montero & Vílchez 2010), the presence of WR stars enriching the ISM (Rivera-Thorsen et al. 2024; Welch et al. 2025), or the details of the star formation history (e.g. Pérez-Montero & Contini 2009; Sanders et al. 2023a). However, Rogers et al. (2024) recently reported a N/O ratio for a galaxy at $z \simeq 3$ consistent with local galaxies (i.e. no evidence for excess N enrichment); a similar result was reported by Berg et al. (2018) from a study of the rest-frame UV spectrum of a lensed galaxy at $z \simeq 2$.

On the other hand, the first estimates of the C/O ratio in SFGs at $z > 6$ (Arellano-Córdova et al. 2022; Jones et al. 2023) have been broadly consistent with the results of low-metallicity SFGs at $z \simeq 0$ (i.e. $12 + \log(O/H) < 8.0$; Berg et al. 2012). For example, Jones et al. (2023) analysed the C/O ratio of a galaxy at $z = 6.23$ using chemical evolution models, concluding that the production of C is consistent with the expectations of pure CCSNe enrichment at low metallicities. Similarly low C/O ratio ratios have been found in galaxies with supersolar N abundances at $z > 6$ (e.g. Curti et al. 2025; Marques-Chaves et al. 2024; Schaerer et al. 2024; Topping et al. 2024b), indicating that while C is consistent with standard nucleosynthesis, an additional source of enrichment seems to be affecting the chemical abundance of N.

However, although most studies report low C/O abundance ratios, evidence of enhanced C enrichment has also been found in a small number of high-redshift sources. For example, Hsiao et al. (2024) analysed the spectrum of a lensed galaxy at $z = 10.17$ (MACS0647-JD) and derived a value of $\log(C/O) = -0.44$, which is somewhat higher than other $z > 6$ estimates (typically between $\log(C/O) = -0.8$ and -1.1; e.g. Jones et al. 2023; Topping et al. 2025, b). These authors concluded that this high value might be due to the high metallicity derived for this object ($12 + \log(O/H) = 7.79$), or the presence of exotic stellar populations (Charbonnel et al. 2023; Watanabe et al. 2024). In addition, while Castellano et al. (2024) (GHZ2; $z = 12.34$) reported a consistent C/O ratio compared to local low-metallicity galaxies, D'Eugenio et al. (2024) (Gs-z12; $z = 12.5$) find a supersolar C abundance that they explain by appealing to the predicted yields of very metal-poor stars. However, an important caveat related to the studies of Castellano et al. (2024) and D'Eugenio et al. (2024) is that they have to assume a value for the electron temperature (T_e) of the gas when deriving abundances. Ultimately, a direct determination of T_e is needed to provide a robust determination of the chemical composition of the gas (e.g. Peimbert, Peimbert & Delgado-Inglada 2017).

A review of the current literature therefore suggests that a coherent picture of the enrichment of C and N in galaxies across all cosmic epochs has not yet emerged. Significant systematic offsets and scatter seem to exist, possibly related to differences in the star formation histories of galaxies, different enrichment mechanisms, variations in the stellar initial mass function (IMF), or observational systematics (e.g. Yan, Jerabkova & Kroupa 2017; Kobayashi et al. 2020; Bekki & Tsujimoto 2023; Curti et al. 2025). To make further progress, additional samples of galaxies with robust estimates of C, N, and O abundances are clearly needed.

In this context, we present an analysis of the ionized gas and physical properties of two SFGs at $z \simeq 5$ observed with *JWST*/NIRSpec. These SFGs are part of the Early eXtragalactic Continuum and Emission Line Science survey (EXCELS; Carnall et al. 2024). Due to the specific redshifts of these sources, they are the only two galaxies from EXCELS for which we can characterize the chemical abundance patterns of C, N, and O. Crucially, in both sources we detect the [O III] $\lambda4363$ auroral line, which probes the gas electron temperature, enabling robust abundance estimates using the direct method. Currently, only four other sources with similar direct estimates of C, N, and O exist in the literature at $z \gtrsim 5$ (Curti et al. 2025; Topping et al. 2025). Our analysis therefore represents a significant increase in direct CNO estimates at early cosmic epochs. By combining the NIRSpec spectra with deep *JWST* PRIMER photometry, we derive the physical properties of these two sources to gain further insight into what drives their chemical enrichment.

This paper is structured as follows. In Section 2, we describe the data reduction of the EXCELS galaxies, and we also describe the additional samples of galaxies across a range of redshifts that we use for comparison. In Section 3, we detail our methodology for the spectral energy distribution fitting, emission-line flux measurements, and the determination of chemical abundances; we also compare the stellar mass and the star formation rate (SFR) as a function of the stellar mass, and investigate the ionization source via BPT diagrams. In Section 4, we present our main results on the C, N, and O abundance patterns by analysing the N/O−, C/O−, and C/N − O/H abundance diagrams. Finally, we summarize our results and present our conclusions in Section 5.

In this paper, we assume a standard cosmological model with $H_0 = 70\,\mathrm{km\ s^{-1}\ Mpc^{-1}}$, $\Omega_m = 0.3$, and $\Omega_\Lambda = 0.7$, and

use the Solar metallicity scale of Asplund, Amarsi & Grevesse (2021), where $12 + \log(O/H)_\odot = 8.69$, $\log(C/O)_\odot = -0.23$, and $\log(N/O)_\odot = -0.86$.

2 DATA

The two galaxies presented here, EXCELS-70864 and EXCELS-121806, were observed as part of the EXCELS Survey (GO 3543; PIs: Carnall, Cullen; Carnall et al. 2024). The EXCELS survey consists of four NIRSpec MSA pointings within the PRIMER UDS field (GO 1837; PI: Dunlop); a detailed description of the survey can be found in Carnall et al. (2024). Here, we briefly summarize the observing strategy and describe the data reduction.

2.1 Observations and data reduction

Each of the four NIRSpec/MSA pointings in EXCELS were observed with the medium-resolution (R $\simeq$ 1000) G140M/F100LP, G235M/F170LP, and G395M/F290LP gratings, and observations were carried out using a 3 shutter slitlet and 3-point dither pattern. For each pointing, the total integration times in each grating were $\simeq$ 4 h in G140M and G395M, and $\simeq$ 5.5 h in G235M, using the NRSIRS2 readout pattern. As described in Carnall et al. (2024), separate MSA configurations were specified for each grating and targets were observed in various combinations of the three gratings. The two objects presented here were observed in all three NIRSpec gratings.[2] At the redshift of these galaxies, the observations covered rest-frame wavelengths $\lambda_{rest} \simeq$ 1600–8500Å, which provides access to a number of key rest-frame UV emission lines such as He II λ1640 and C III] $\lambda\lambda$1906,1909 and several rest-frame optical lines such as [O II] λ3726,3727, Hβ, [O III] λ4363, Hα, and [N II] $\lambda\lambda$6548,6584.

The raw data were reduced using v1.15.1 of the *JWST* reduction pipeline.[3] We adopted the default level 1 configuration except for turning on advanced snowball rejection and using the CRDS_CTX = jwst_1258.pmap version of the *JWST* Calibration Reference Data System files. We then ran the level 2 pipeline steps assuming the default configuration. Finally, the level 3 pipeline was used to combine the 2D spectra that were then used for science analysis. We then performed our own custom 1D optimal extraction of the 2D spectra (Horne 1986), setting the extraction centroid as the flux-weighted mean position of the object within the NIRSpec/MSA slitlet (see Carnall et al. 2024).

We performed flux calibration by first matching the flux level between the different gratings. To do this, we calculated the median flux in overlapping wavelength regions and scaled the G140M and G395M spectra to the overlapping regions of the G235M spectra. To achieve an absolute flux calibration, we then scaled the full spectra to the overlapping broad-band photometry. Each galaxy in the EXCELS sample benefits from deep *HST* and *JWST*/NIRCam imaging spanning the wavelength range 0.4–5μm in 11 photometric bands: *F435W*, *F606W*, *F814W*, *F090W*, *F115W*, *F150W*, *F200W*, *F277W*, *F356W*, *F410M*, and *F444W*. The broad-band fluxes are extracted from the PSF-homogenized images using 0.5 arcsec diameter apertures and corrected to total using the *F356W* FLUX_AUTO values measured by SOURCEEXTRACTOR (Bertin &

Arnouts 1996). We integrated each spectrum through the appropriate overlapping filters and scaled them to the corresponding photometry. The final correction as a function of wavelength is derived via a linear interpolation between the bands. Figs 1 and 2 show the final rest-frame UV-to-optical spectra for EXCELS-70864 and EXCELS-121806. From the multiple emission lines visible in these figures, we measure spectroscopic redshifts of $z = 5.255$ and $z = 5.225$, respectively.

2.2 Additional SFG samples

To supplement our analysis, we have also gathered a sample of SFGs across a range of cosmic epochs with the aim of comparing their properties and chemical patterns with our EXCELS galaxies at $z \simeq 5$. For this literature selection, we have only considered galaxies that have robust C, N, and O abundance determinations using the T_e-sensitive method.

This comparison sample includes dwarf SFGs at $z \simeq 0$ from Berg et al. (2012), Berg et al. (2016), Berg et al. (2019a), Izotov et al. (2023), and Flury et al. (2022). In particular, we have incorporated galaxies from the COS Legacy Archival Spectroscopic SurveY (Berg et al. 2022; James et al. 2022; Arellano-Córdova et al. 2024; CLASSY), which spans a wide range in ISM conditions and physical properties (e.g. stellar mass, SFR, and ionization parameter). The CLASSY galaxies span a metallicity range of $12 + \log(O/H) = 7.9$–8.8 and represent our primary local analogue sample. We have taken the results of C and N from Martinez et al. in preparation and Arellano-Córdova et al. in preparation, respectively. Additionally, we have also included the $z \simeq 0$ Lyman continuum emitting (LCE) galaxies from Izotov et al. (2023); as discussed in Izotov et al. (2023), these galaxies appear to show a distinct CNO abundance pattern compared to non-LCE galaxies (e.g. Berg et al. 2012), which may help to interpret the abundance patterns being observed at higher redshifts.

Along with the local sample, we have also compiled measurements of the physical properties and direct CNO chemical abundances for a sample of galaxies in the redshift range $z = 2$–10 taken from a number of literature sources (Berg et al. 2018; Llerena et al. 2023; Marques-Chaves et al. 2023; Sanders et al. 2023a; Isobe et al. 2023b; Citro et al. 2024; Curti et al. 2025; Hsiao et al. 2024; Hu et al. 2024; Morishita et al. 2024; Rogers et al. 2024; Schaerer et al. 2024; Shapley et al. 2025; Topping et al. 2025. In total, our comparison sample comprises measurements of C, N, and O abundances with metallicities ranging between $12 + \log(O/H) = 7.12$ and 8.8. We note that we have used abundance patterns directly from the original papers and not attempted to recalculate them in this work. We have also compiled the galaxy properties, such as stellar mass and SFR, as reported by the original authors when these values are available; where necessary, we have converted the values to a Kroupa (2001) IMF for consistency with our analysis. In Table 1, we list the chemical abundance determinations for this $z \gtrsim 2$ literature sample.

3 CHEMICAL ABUNDANCES AND PHYSICAL PROPERTIES

In this section, we present our analysis of the *JWST* data for the two galaxies at $z \simeq 5$. We first describe the measurement of emission-line fluxes from the NIRSpec data. These flux measurements then allow us to determine the reddening due to dust, the ionization source, SFR, physical conditions of the ISM (T_e and n_e), and the chemical abundances. We finally describe how the stellar mass

---

[2]Because independent MSA configurations were used for each grating, there are small variations in the slit position with respect to the galaxy centroid between the gratings. However, these shifts are negligible for the two objects presented here.

[3]https://github.com/spacetelescope/jwst
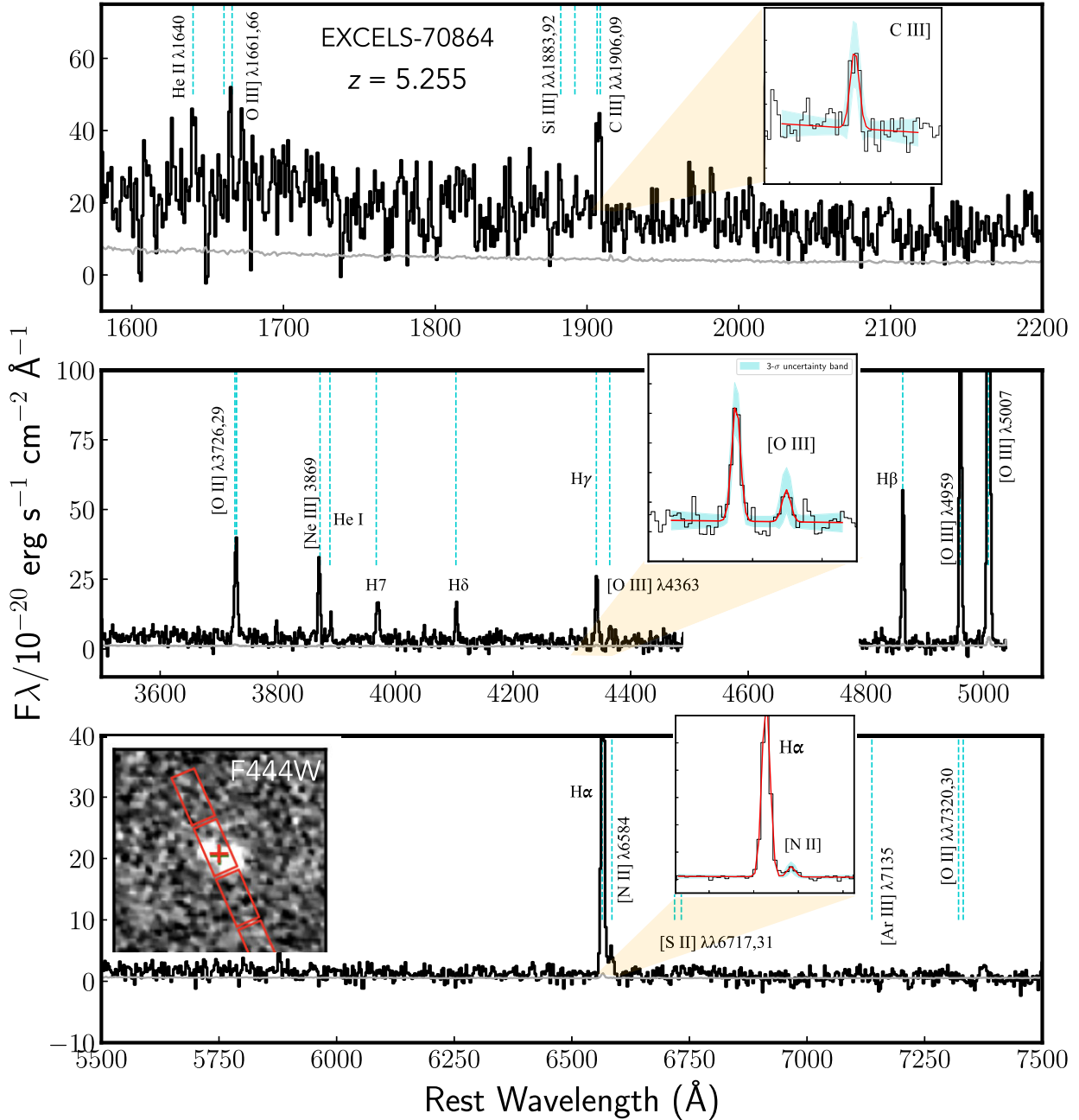
Figure 1. Rest-frame UV and optical NIRSpec spectra of EXCELS-70864 at $z = 5.255$. The black and grey lines show the spectrum and error spectrum, respectively. We highlight the detection of some UV and optical features such as C III] λ1906,1909, [O II] $\lambda\lambda$3726,29, [Ne III] λ3869, [O III] λ4363, [N II] λ6584, and [S II] $\lambda\lambda$6717,31, which are used to determine the physical conditions, chemical abundances, and physical properties of EXCELS-70864. The insert figures show the emission-line fitting of C III] λ1906,1909, [O III] λ4363, and [N II] λ6584, which are essential to calculate the C and N abundances using the T_e sensitive method. The emission-line fits are shown in red and the uncertainties are shown by the light blue shaded region. The bottom panel shows the *F*444*W* imaging and the slit position of the G235M grating. The crosses indicate the galaxy centre (green) and the slit centre (red) (see also Carnall et al. 2024).

of these galaxies was estimated from fitting to the emission-line corrected broad-band photometry.

3.1 Emission-line measurements

The emission-line fluxes are measured following the methodology of Scholte et al. (2025) and Stanton et al. (2025). Here, we include a short summary of that procedure. All the emission lines are fitted

using Gaussian line profiles after continuum subtraction using a common intrinsic line width and line velocity. The line amplitude is freely fitted for each emission line. The continuum flux is estimated using a running mean of the 16th to 84th percentile flux values within a top hat function with a rest-wavelength width of 350 Å. In Section 3.5, we provide a brief discussion on continuum subtraction fitting based on SED fitting. Details of the procedure can be found in Scholte et al. (2025). For the C III] $\lambda\lambda$1907,09 and [O II] $\lambda\lambda$3727
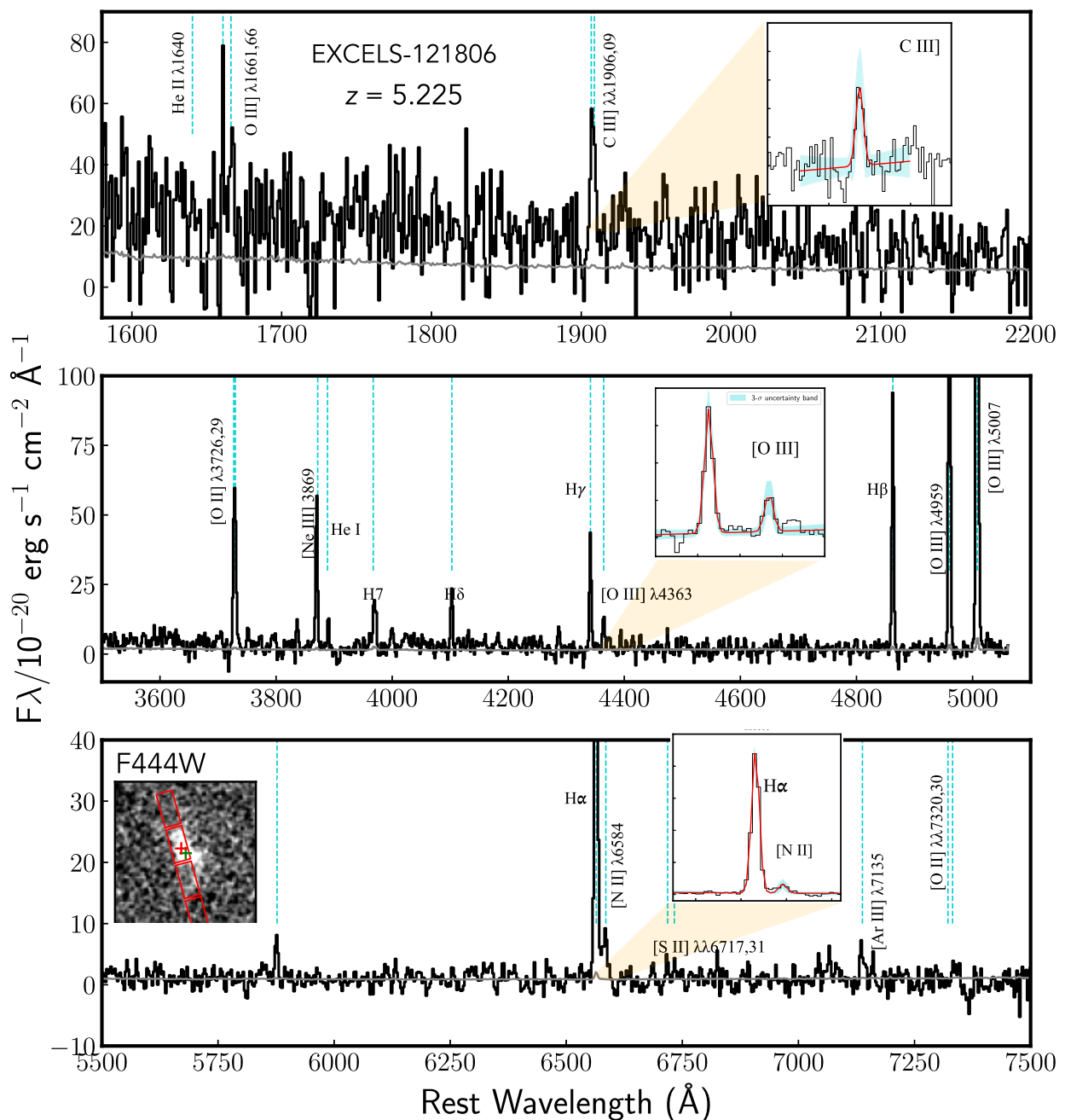
Figure 2. Rest-frame UV and optical NIRSpec spectra of EXCELS-121806 at $z = 5.255$. For more details see Fig. 1.

doublets, we have modelled the flux as the sum of the two Gaussian components. The intrinsic line widths of the individual emission lines are tied to the other emission lines. Total line widths are then also convolved with the wavelength-dependent resolution of the grating.

To re-estimate the flux uncertainties we use the continuum-subtracted residuals by implying a multiplication factor to the pipeline flux uncertainties such that $\tilde{\sigma}_F = \frac{1}{2}(R_{84} - R_{16})$, where $\tilde{\sigma}_F$ is the median flux uncertainty and R_{16} and R_{84} are the 16th and 84th percentiles of the residuals. The emission-line flux uncertainties are calculated using a line profile weighted average of the pixel flux uncertainties (e.g. Moustakas et al. 2023). As discussed in Scholte et al. (2025), we find an excess scatter (i.e. after accounting for the statistical uncertainties) in line flux measurements of the same emission lines in multiple gratings of $\simeq 8$ per cent. Throughout this

paper, this additional calibration uncertainty is included in any line ratio measured using lines measured in different gratings. The inset panels in Figs 1 and 2 show some examples of the fitting for C III] $\lambda\lambda 1906,09$, the T_e-sensitive [O III] $\lambda 4363$ line, and [N II] $\lambda 6584$ for the two galaxies in this analysis (these are the three crucial lines required to simultaneously measure C, N, and O abundances). In Table 2, we present the fluxes and corresponding uncertainties of the emission lines analysed in this paper.

3.2 Nebular dust reddening

We first compared the observed and theoretical values of the Balmer line ratios to assess the magnitude of dust reddening in EXCELS-70864 and EXCELS-121806 (Osterbrock 1989; Osterbrock & Fer-

Table 1. A compilation of SFGs at $z \geq 2$ with measurements of the metallicity (O/H), N/O, and C/O abundance ratios derived using the T_e-sensitive method. Columns 1 and 2 give the galaxy ID and its redshift, while columns 3–6 give the metallicity and the C/O and N/O abundance ratios. For N/O, we have separated the results based on whether UV N lines or optical N lines were used to derive the abundance ratio (columns 5 and 6). Column 7 provides the references for the original studies.

Galaxy	z	12+log(O/H)	log(C/O)	log(N/O)$_{\rm opt}$	log(N/O)$_{\rm UV}$	Reference
SL2S J0217-0513	1.84	≥ 7.50	-0.81 ± 0.09	–	-1.48 ± 0.46	Berg et al. (2018)
ID_19985	2.19	7.89 ± 0.20	–	-0.69 ± 0.10	–	Sanders, Jones & others (2023a)
ID_20062	2.19	8.24 ± 0.27	–	-0.78 ± 0.14	–	Sanders et al. (2023a)
Sunburst Arc	2.37	7.97 ± 0.05	–	$-0.65^{+0.16}_{-0.25}$	–	Welch et al. (2025)
Q2343-D40	2.96	8.07 ± 0.06	–	-1.37 ± 0.21	–	Rogers et al. (2024)
J0332-3557	3.77	8.26 ± 0.06	-1.02 ± 0.20	–	–	Citro et al. (2024)
RXCJ2248-ID	6.11	7.43 ± 0.17	-0.83 ± 0.11	$-0.60 \pm 0.15\,^{a}$	-0.39 ± 0.11	Topping et al. (2024b)
A1703-zd6	7.04	7.47 ± 0.19	-0.70 ± 0.18	–	-0.60 ± 0.30	Topping et al. (2025)
CEERS_1019	8.63	7.70 ± 0.18	-0.75 ± 0.11	–	-0.18 ± 0.28	Marques-Chaves et al. (2024)
GLASS_15008	6.23	7.39 ± 0.23	-1.01 ± 0.12	–	–	Jones et al. (2023)
GLASS_15008	6.23	$7.65^{+0.14}_{-0.08}$	$-1.08^{+0.06}_{-0.14}$	–	$-0.40^{+0.05}_{-0.07}$	Isobe et al. (2023a)
ERO*S*_04590	8.49	7.12 ± 0.12	-0.83 ± 0.38	–	–	Arellano-Córdova et al. (2022)
GN-z9p4	9.38	7.37 ± 0.15	> -1.18	–	-0.59 ± 0.24	Schaerer et al. (2024)
GS-z9-0	9.43	7.40 ± 0.09	-0.93 ± 0.24	–	-0.90 ± 0.24	Curti et al. (2025)
MACS0647-JD	10.17	7.79 ± 0.09	$-0.44^{+0.06}_{-0.07}$	–	–	Hsiao et al. (2024)
EXCELS-121806	5.225	$7.97^{+0.05}_{-0.04}$	-1.02 ± 0.22	$-0.87^{+0.14}_{-0.11}$	–	This Work
EXCELS-70684	5.255	$8.21^{+0.08}_{-0.05}$	-0.82 ± 0.22	$-1.07^{+0.17}_{-0.12}$	–	This Work

Note. ^{a} Optical N/O abundance that we have derived in this study using the flux measurements and the physical conditions reported in Topping et al. (2024b).

Table 2. Emission-line fluxes for the two EXCELS galaxies at $z \simeq 5$.

Line	70864 Flux [10^{-19} erg s^{-1} cm^{-2}]	121806 Flux [10^{-19} erg s^{-1} cm^{-2}]
[He II] $\lambda 1640$	8.18 ± 2.36	< 2.96
[O III] $\lambda 1666$	< 6.79	9.44 ± 3.10
[C III] $\lambda\lambda 1907,09^{a}$	11.55 ± 2.07	16.06 ± 3.21
[O III] $\lambda\lambda 3727$	21.90 ± 1.30	34.10 ± 1.50
[Ne III] $\lambda 3869$	14.44 ± 0.78	23.58 ± 1.03
Hδ	6.42 ± 0.69	9.63 ± 0.08
Hγ	12.28 ± 0.88	17.29 ± 0.93
[O III] $\lambda 4363$	2.84 ± 0.69	5.43 ± 0.84
Hβ (G235M)b	28.26 ± 1.01	39.49 ± 1.15
[O III] $\lambda 4959$	73.18 ± 1.45	94.32 ± 1.46
[O III] $\lambda 5007$	220.94 ± 2.26	276.74 ± 2.30
Hβ (G395M)b	25.64 ± 1.13	40.54 ± 1.36
Hα	64.13 ± 1.13	103.03 ± 1.42
[N II] $\lambda 6584$	2.77 ± 0.56	6.78 ± 0.72
[S II] $\lambda 6717$	< 1.00	2.4 ± 0.75
[S II] $\lambda 6731$	< 1.14	1.96 ± 0.72
[Ar III] $\lambda 7135$	< 0.74	4.77 ± 0.90

Notes. ^{a} C III] $\lambda 1907$ + [C III] $\lambda 1909$.
b Hβ (G235M) and Hβ (G395M) correspond to the flux measured from each grating.

land 2006). For both galaxies, we have used the following Balmer ratios: Hδ/Hβ, Hγ/Hβ, and Hα/Hβ. Although higher order Balmer lines are also detected in both spectra (e.g. Hϵ, Hζ, and Hη), we decided to omit these lines due to the contamination from nearby emission lines and large uncertainties on their fluxes. We assumed Case B recombination corresponding to theoretical values of Hγ/Hβ = 2.78, Hγ/Hβ = 0.47, and Hδ/Hβ = 0.26, which we calculated using the PyNeb package (Luridiana, Morisset & Shaw 2015) for T_e = 15,000 K and n_e = 300 cm^{-3}.

In Fig. 3, we report the observed Balmer ratios compared to the range of expected theoretical values computed for temperatures between T_e = 10,000 − 20,000 K (red rectangles). For both galaxies, we do not find strong evidence for inconsistencies with the theoretical ratios within the uncertainties. In both cases, there is evidence for minor amounts of dust reddening in their Hγ/Hβ and Hδ/Hβ ratios, albeit in both cases the ratios are consistent with $E(B-V) = 0$. Interestingly, however, both galaxies show a value of Hα/Hβ *below* the theoretical ratio. These anomalous ratios that fall systematically below the expected value are becoming relatively common in *JWST* spectra at high redshifts (e.g. Yanagisawa et al. 2024). To highlight this, we have also added in Fig. 3 two other $z > 6$ galaxies which show anomalous Hα/Hβ ratios from Topping et al. (2024b) (RXCJ2248-ID) and Cameron et al. (2023) (GS-NDG-9422). We note that low values of Hα/Hβ have also been reported in galaxies at low-redshift (Kewley, Jansen & Geller 2005; Scarlata et al. 2024).

Investigation of these anomalous values of Hα/Hβ have been conducted in Yanagisawa et al. (2024) and McClymont et al. (2024) for galaxies at $z > 6$ and by Scarlata et al. (2024) for galaxies at $z \simeq 0$. For example, McClymont et al. (2024) analysed the cause of anomalous Hα/Hβ and Hγ/Hβ ratios using 19 galaxies from JADES. With the aid of photoionization models, these authors conclude that a density-bounded nebula is one of the possible explanations for the anomalous ratios. It is unclear whether EXCELS-70864 and EXCELS-121806 are consistent with density-bounded nebulae, although we note the [O III] $\lambda 5007$/[O II] $\lambda 3726,3727$ ratios are not particularly extreme (Table 2).

Since all ratios are consistent within 2σ of their Case B values, we have assumed that the anomalous Balmer ratios are most likely due to statistical scatter in our case. From the Hγ/Hβ and Hδ/Hβ ratios, we estimate $E(B-V) = 0.19 \pm 0.11$ for EXCELS-70864 and $E(B-V) = 0.13 \pm 0.08$ for EXCELS-121806. As both of these values are consistent with $E(B-V) = 0$ within the uncertainties, and the Hα/Hβ ratios also indicate zero/negligible dust attenuation, in the following analysis, we have used the observed fluxes without dust correction. Reassuringly, we find that in the case of zero reddening, the physical conditions derived for EXCELS-121806
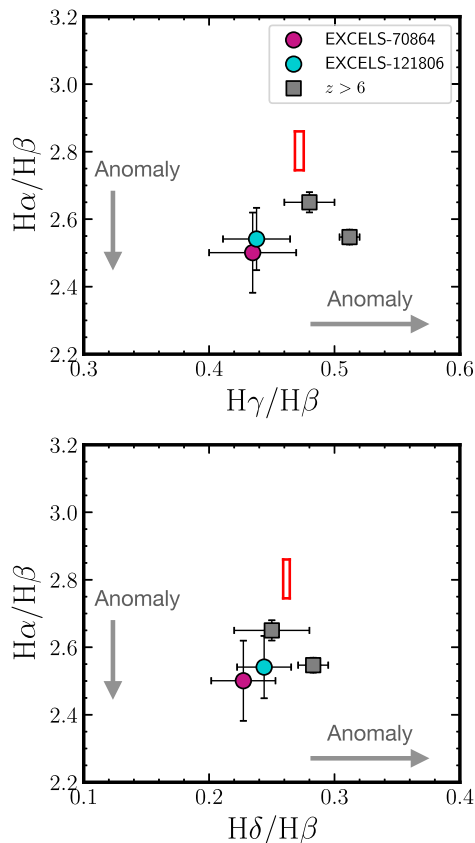
Figure 3. The observed Balmer ratios of the EXCELS galaxies at $z \simeq 5$. The red rectangles represent the theoretical Balmer ratios under the conditions of $T_e = 10\,000\,$–$\,20\,000$ K and $n_e = 300\,\mathrm{cm}^{-3}$. *Top panel*: H$\alpha$/H$\beta$ versus Hγ/Hβ. Both galaxies display Hα/Hβ ratios below the Case B value, while the Hγ/Hβ ratios are consistent with the Case B value or a small amount of nebular reddening. *Bottom*: Hα/Hβ versus Hδ/Hβ. Again the EXCELS galaxies Hδ/Hβ ratios consistent with the theoretical value within the uncertainties. The grey squares represent the measurements of galaxies at $z \sim 6$ taken from Topping et al. (2024b) and Cameron et al. (2023). The arrows indicate the direction in which the Balmer ratios become anomalous with respect to the Case B theoretical values (i.e. not consistent with the dust-free Case B ratios). Consistent with other results in the literature, we find that both galaxies display sub-Case B Hα/Hβ ratios. However, all Balmer line ratios are consistent with the zero-reddening Case B ratios within the 2σ uncertainties.

using the optical [O III] λ4363 line and UV [O III] λ1666 line are fully consistent (see Table 3). We therefore argue that the assumption of zero reddening is an appropriate for our analysis. In Section 4, we discuss the impact of dust uncertainties on the C/O and N/O abundance ratios.

3.3 Evidence for AGN ionization?

We investigated whether the observed line ratios are compatible with pure star formation or whether there is evidence for AGN ionization in either of our sources. emission-line ratio diagnostics can help us to discern how the gas in galaxies is being ionized (e.g. star formation, AGN or shocks; Baldwin, Phillips & Terlevich 1981; Kewley et al. 2001; Kauffmann et al. 2003; Allen et al. 2008; Mingozzi et al. 2024). In Fig. 4, we show the [N II]/Hα (left) and [S II]/Hα (right) BPT diagrams for our two EXCELS galaxies; we also include the additional sample of local and high-redshift galaxies for comparison.

Table 3. The physical properties and chemical abundances derived for the two $z \simeq 5$ EXCELS galaxies.

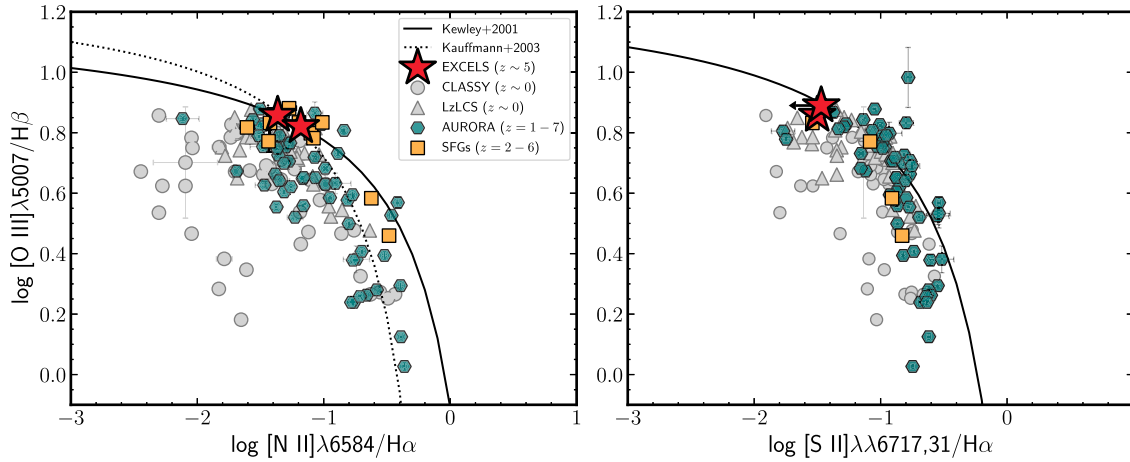|	EXCELS	
Galaxy properties	70864	121806
$\log \mathrm{M}_\star$ ($\mathrm{M}_\odot$)	$8.09^{+0.24}_{-0.15}$	$8.02^{+0.06}_{-0.08}$
$\log(\mathrm{SFR})$ (Hα) [$\mathrm{M}_\odot\,\mathrm{yr}^{-1}$]	0.79 ± 0.01	1.00 ± 0.01
$\log(\mathrm{SFR})$ (SED) [$\mathrm{M}_\odot\,\mathrm{yr}^{-1}$]	$0.97^{+0.09}_{-0.07}$	1.02 ± 0.07
n_e[S II] [cm^{-3}]	–	600^{+920}_{-400}
T_e[O III] [K]	12500^{+1100}_{-1300}	14900 ± 1100
T_e[O III] (UV)[a] [K]	–	15300 ± 1250
12+log(O/H)	$8.21^{+0.08}_{-0.05}$	$7.97^{+0.05}_{-0.04}$
log(C/O)	-0.82 ± 0.22	-1.02 ± 0.22
log(C/O) (UV)[a]	–	-1.07 ± 0.43
log(N/O)	$-1.07^{+0.17}_{-0.13}$	$-0.86^{+0.15}_{-0.11}$
log(Ne/O)	-0.70 ± 0.16	-0.63 ± 0.11
log(Ar/O)	–	-2.20 ± 0.28
EW(Hβ)b [Å]	112 ± 13	176 ± 16

Notes. O32 = [O III]/[O II] (a proxy for the the ionization parameter).
[a] In these cases, the T_e[O III] and C/O were determined using the T_e UV-diagnostic of O III λ1666/[O III] λ5007 and the C III λ1909/O III λ1666 line ratio, respectively. Reassuringly, in both cases the values are fully consistent with value derived using the optical [O III] λ4363 line. b EW(Hβ) in the rest frame.

It can be seen from Fig. 4 that both of the EXCELS galaxies are located close to the limit of the region of pure star formation defined by the Kewley et al. (2001) and Kauffmann et al. (2003) demarcation lines (dotted and solid lines, respectively). The same is true for most of the other galaxies at $z > 2$ (squares), and indicates very high-ionization objects. We also show the [S II]-BPT diagram for one of our galaxies, EXCELS-121806, which has a robust detection of the [S II] $\lambda\lambda$6717,31 doublet (see right panel of Fig. 4), finding a consistent picture in which the line ratios fall close to the star formation limit. For EXCELS-70864, we used the upper limits of the [S II] $\lambda\lambda$6717, 31 fluxes to estimate the [S II]/Hα ratio. Overall, we find no strong evidence to suggest that the gas in either galaxy is being ionized by an AGN. Moreover, the spectra of these two galaxies do not show evidence for broad or multiple Gaussian components.

It can be seen from Fig. 4 that the high-redshift samples are systematically offset from the local analogue sample; this is a well-studied problem (Steidel et al. 2014; Shapley et al. 2015, 2025) that can be attributed, at least in part, to the α-enhanced abundance ratios that appear to be ubiquitous in the $z > 2$ star-forming population (e.g. Steidel et al. 2016; Cullen et al. 2019, 2021; Topping et al. 2020; Stanton et al. 2024). At fixed α-element abundance, high-redshift galaxies are expected to have systematically lower Fe abundances and therefore harder ionizing spectra. These line ratio diagrams therefore offer the first piece of evidence that our $z \simeq 5$ galaxies likely differ from the local analogues in terms of their ionization state and chemical abundances.

The rest-frame UV lines are another alternative way to distinguish between star formation and AGN-driven ionization in galaxies (Curti et al. 2025; Mingozzi et al. 2024; Topping et al. 2025, b). In addition to the UV carbon lines, we also have measurements of He II λ1640 (S/N $\geq$ 3) for EXCELS-70864. However, we are missing the detection of the O III] $\lambda\lambda$1661,66 doublet, which makes it difficult to analyse any UV-diagnostic (e.g. Flury et al. 2024; Mingozzi et al. 2024). In future work, we plan to characterize the ionization source for the full EXCELS sample in greater detail.

Figure 4. The [N II] (left) and [S II] (right) BPT diagrams for the EXCELS galaxies and a selection of literature samples. For EXCELS-70864, we have determined an upper limit for [S II]/Hα. The solid line shows the theoretical maximum starburst separation of Kewley et al. (2001), while the dashed line illustrates the boundary between star formation and AGN from Kauffmann et al. (2003). The orange squares show a sample of galaxies at high redshift with [N II] and [S II] detections from Sanders et al. (2023a) ($z \simeq 2$), Sanders et al. (2024) ($z \simeq 2$–4), Rogers et al. (2024) ($z = 2.96$), Welch et al. (2025) ($z = 2.37$), and Topping et al. (2024b) ($z = 6.11$). The turquoise hexagons show data from the AURORA survey at $z = 1$–7 (Shapley et al. 2025). The grey symbols represent the CLASSY survey (Berg et al. 2022; Mingozzi et al. 2024) and SFGs from the Lyman Continuum Survey (Flury et al. 2022). The two EXCELS galaxies display similar line ratios to the other $z > 3$ galaxies, which are also consistent with the local comparison samples. There is no obvious evidence for AGN ionization based on these optical emission-line ratios.

3.4 Physical conditions and chemical abundances

3.4.1 Electron density and temperature

The electron temperature (T_e) and density (n_e) for EXCELS-70864 and EXCELS-121806 were determined using the nebular analysis package PYNEB (Luridiana et al. 2015; version 1.1.14) using the same atomic data reported in Arellano-Córdova et al. (2024). All atomic data assume a five-level atom model (De Robertis, Dufour & Hunt 1987) with the exception of O that uses a six-level atom. For C, we use the transition probabilities of Glass (1983), Nussbaumer & Storey (1978), and Wiese, Fuhr & Deters (1996) and the collision strengths of Berrington et al. (1985).

We have used the [O III] $\lambda4363/\lambda5007$ and [S II] $\lambda6717/\lambda6731$ line ratios to calculate T_e[O III] and n_e[S II], respectively. For EXCELS-121806, we have also calculated T_e[O III] using the UV auroral line [O III] $\lambda1666$ via the [O III] $\lambda1666/\lambda5007$ ratio. The electron density is only constrained for EXCELS-121806, for which we find a value of $n_e = 600^{+920}_{-400}$ cm^{-3}; we adopted the same value for EXCELS-70864. In Table 3, we report the electron density and temperature for both galaxies. We find values of T_e[O III]$= 12500^{+1100}_{-1300}$ K and T_e[O III]$= 14900 \pm 1100$ K for EXCELS-70868 and EXCELS-121806, respectively. Our constraint on T_e[O III] using the UV+optical line ratios is also in agreement with the result using only optical lines, T_e[O III] (UV) $= 15300 \pm 1250$ K. These values are consistent with the inferred T_e in the CLASSY low-redshift analogue sample (e.g. Mingozzi et al. 2022; Arellano-Córdova et al. 2024). In this study, we used the result obtained for T_e[O III] using optical lines to derive the ionic abundances.

3.4.2 Ionic and total abundances

We have defined a three ionization zone temperature structure to determine the ionic chemical abundances. We use T_e[O III] as representative of the high-ionization zone, and T_e[O II] (or T_e[N II]) and T_e[S III] as a representative of the low and intermediate ionization zones, respectively. However, T_e[O II], T_e[N II] and T_e[S III] are not

available in this sample. Therefore, we have used temperature relations to estimate the low- and intermediate- ionization zone temperatures. We have estimated T_e[O II] using the temperature relation reported in Arellano-Córdova & Rodríguez (2020), which is based on observational data and accounts for the dependency on the ionization parameter. To estimate T_e[S III], we have used the temperature relation of Garnett (1992), which is based on the photoionization models of Stasińska (1982). Similar relations are used in many other studies of both local and high-redshift galaxies throughout the literature (e.g. Kennicutt, Bresolin & Garnett 2003; Arellano-Córdova & Rodríguez 2020; Berg et al. 2022; Arellano-Córdova et al. 2024; Hu et al. 2024; Rogers et al. 2024).

Based on the estimates of T_e and n_e, we then derived the element abundances relative to hydrogen using the emission-line fluxes of the various ions observed in the EXCELS spectra. In addition to C, N, and O, which are the main focus of this work, we also determined Ne and Ar abundances using the [$Ne\,iii$] $\lambda3869$ and [$Ar\,iii$] $\lambda7135$ lines where available (Table 2) which we will discuss briefly below. We computed the ionic abundance of low-ionization species (N$^+$ and O$^+$) using T_e[O II], intermediate-ionization species (Ar^{2+}) using T_e[S III], and high-ionization species (C^{2+}, O^{2+}, and Ne^{2+})[4] using T_e[O III] (e.g. Garnett 1992; Jones et al. 2023). For O, we also derived the ionic abundance of O^{2+} using O III $\lambda1666$ and [O III] $\lambda5007$.

These ionic abundances were then converted to total element abundance using various prescriptions. For O, the total abundance was calculated by summing the contribution of O$^+$/H$^+$ and O^{2+}/H$^+$. The contribution of O^{3+}/H$^+$ is expected to be minimal even in highly ionized environments and therefore we do not consider any additional ionization correction factor (ICF; Berg

---

[4] T_e[S III] is also used to infer C^{2+} due to the similarity in ionization potentials between S^{2+} (23–35 eV) and C^{2+} (24–48 eV). We recalculated the C/O ratios using T_e[S III] finding differences smaller than 0.09 dex compared to the values reported in Table 3. These differences lie within the uncertainties associated with the C/O ratios derived using T_e[O III] (see also Garnett 1992; Jones et al. 2023).

et al. [2021]). We derive total gas-phase oxygen abundances (i.e. metallicities) of $12 + \log(\text{O/H}) = 8.21^{+0.07}_{-0.05}$ for EXCELS-70864 and $12 + \log(\text{O/H}) = 7.96^{+0.05}_{-0.04}$ for EXCELS-121806. These values translate into metallicities of $Z \simeq 0.3\,Z_\odot$ and $Z \simeq 0.2\,Z_\odot$ respectively. As discussed below, these estimates are at the upper end of the derived values for other galaxies at $z \gtrsim 5$ in the literature (e.g. Isobe et al. [2023b]; Morishita et al. [2024]).

For all of the other elements, we used the ICFs to take into account the contribution of the unobserved ions. For N, we have used the ICF proposed by Peimbert & Costero ([1969]), which is based on the similarity of the ionization potentials of N^+ and O^+, such that $\text{N}^+/\text{O}^+ \approx \text{N/O}$. To derive the total C abundances, we use the ICF of Berg et al. ([2022]), which is valid for high-ionization galaxies, and has been used in other studies at high redshift (e.g. Arellano-Córdova et al. [2022]; Jones et al. [2023]; Citro et al. [2024]). Recently, Izotov et al. ([2023]) provided a bespoke ICF for C based on the properties of LCE at $z = 0$; we also tested this ICF, and obtained very similar results with a difference of only 0.03 dex. For Ne and Ar, we follow the recommendation of Arellano-Córdova et al. ([2024]) who analysed the ICFs for several ions using the CLASSY sample at $z \simeq 0$ and recommend the ICFs of Dors et al. ([2013]) for Ne, and Izotov et al. ([2006]) for Ar.

To calculate the uncertainties associated with the ISM conditions and chemical abundances, we used Monte Carlo simulations generating a Gaussian distribution of 1000 random values. The final values are taken as the median of the resulting distribution, and the reported uncertainties are determined from the 16th and 84th percentiles. Additionally, we have added in quadrature an uncertainty of 610 and 1300 K to the estimated of $T_e[\text{S\,III}]$ and $T_e[\text{O\,II}]$, respectively (e.g. Rogers et al. [2021]; Stanton et al. [2025]). The abundances and corresponding uncertainties for our two $z \simeq 5$ galaxies are reported in Table [3].

3.4.3 Neon and argon abundances

We also report the Ne/O and Ar/O abundance ratios in Table [3]. Our derived values for Ne/O are in excellent agreement with the Solar ratio ($\log(\text{Ne/O})_\odot = -0.63$) and with the average value of $\log(\text{Ne/O}) = -0.63 \pm 0.06$ reported Arellano-Córdova et al. ([2024]) for the $z \simeq 0$ CLASSY sample (see also Izotov et al. [2006]; Berg et al. [2019a]). Furthermore, a solar-like Ne/O has also been reported for a number of other high-redshift samples (e.g. Arellano-Córdova et al. [2022]; Marques-Chaves et al. [2024]; Schaerer et al. [2024]). Indeed, a solar-like Ne/O ratio is expected at high redshifts as both are α-elements, and their ratio at low metallicities should be determined by the CCSNe yields of massive stars (Kobayashi et al. [2020]). The consistency of our data with the Solar value, and with other local and high-redshift systems, is therefore reassuring evidence that our flux calibration and dust corrections are likely to be reasonable.

For EXCELS-121806 we have a measurement of the [Ar\,III] $\lambda 7135$ line from which we derived a value of $\log(\text{Ar/O}) = -2.20 \pm 0.28$ using the ICF of Izotov et al. ([2006]). This value is slightly higher than observed in local SFGs (e.g. Izotov et al. [2006]; Arellano-Córdova et al. [2024]); for example, the mean value reported for the CLASSY galaxies is $\log(\text{Ar/O}) = -2.33 \pm 0.09$ (Arellano-Córdova et al. [2024]), which is consistent with the Solar value of Asplund et al. ([2021]). To check the dependence on the ICF, we also used the ICF of Pérez-Montero et al. ([2007]) which yields a lower value $\log(\text{Ar/O}) = -2.40 \pm 0.28$, but is still fully consistent within the uncertainties. In a companion work, Stanton et al. ([2025]) determined the average Ar/O abundance ratio for nine EXCELS galaxies

$z = 3 - 5$ (which includes EXCELS-121806) finding a weighted average value of $\langle \log(\text{Ar/O}) \rangle = -2.52 \pm 0.07$, consistent with an Ar deficit due to the delay in Type Ia supernovae enrichment at high redshifts. Given the large uncertainty, it is difficult to draw any firm conclusions from this single $z = 5$ Ar/O abundance measurement, but the value we derive is clearly within the range of expected values. Finally, we revised the dependence of abundance determinations on electron density by varying $n_e = 10^2$-10^4 cm^{-3}. High electron densities have been reported both locally and at high-z using various UV diagnostics that trace different density gas structure within the nebula (e.g. Mingozzi et al. [2022]; Topping et al. [2024b]). Overall, we find that variations in O/H, C/O, Ne/O, and Ar/O remain below 0.1 dex compared to the values reported in Table [3]. For N/O, we note a large discrepancy in such a ratio with a difference of 0.33 dex by assuming $n_e = 10^4$ cm^{-3}. Such high densities cannot be confirmed as we lack detections of other diagnostics that trace high-density diagnostics such as [Ar\,IV] $\lambda 4711,41$, while that C\,III] $\lambda\lambda 1906,09$ is blended (see Fig. [1]).

3.4.4 A comparison to strong-line methods

It is perhaps useful to consider what values of O/H, N/O and C/O we would obtain if we did not have an estimate of the electron temperature and had to instead rely on empirical strong line methods. To do this, we first inferred the metallicity of EXCELS-70864 and EXCELS-121806 using the strong-line calibrations of Sanders et al. ([2024]), which were derived using a sample of galaxies at $z = 2 - 9$ with T_e-measurements. We used the emission-line ratios O2 ($=$[O\,II]/Hβ), O3 ($=$[O\,II]/Hβ), R23 ($=$([O\,II] + [O\,III])/Hβ), O32 ($=$[O\,III]/[O\,II]), and Ne3O2 ($=$[Ne\,III]/[O\,III]). We did not consider calibrations using the [N\,II] line due to their secondary dependence on the N/O ratio (e.g. Arellano-Córdova & Rodríguez [2020]). We averaged the metallicities derived from the different calibrators to compare with the results of the direct method. For EXCELS-121806, we find $12 + \log(\text{O/H}) = 7.92$, which is 0.05 dex lower than the value obtained using the T_e-sensitive method but fully consistent within the uncertainties (see Table [3]). For EXCELS-70864, we infer $12 + \log(\text{O/H}) = 7.87$, which is 0.34 dex lower than our T_e-based estimate. We have also checked that applying the reddening correction of $E(B - V) = 0.19$ derived from the higher order Balmer lines for EXCELS-70864 results in a similar offset. This offset is larger than the scatter on the O2, O3, Ne3O2, O32, and R23 methods (Sanders et al. [2024]) and highlights the fact that strong line methods are likely to artificially reduce the true scatter in abundance measurements at high redshifts and are not reliable when applied to individual objects.

3.5 Stellar masses and SFRs

To estimate stellar masses and SFRs, we fitted the broad-band photometry of the two EXCELS galaxies using the BAGPIPES SED fitting code (Carnall et al. [2018], [2019]). In addition to the *HST* and *JWST*/NIRCam photometry described above, EXCELS-121806 falls within the PRIMER/MIRI region and therefore benefits from additional *JWST*/MIRI 7.7 μm photometry which we also include in the SED fitting for this object. We first subtracted the measured emission-line fluxes from the photometric data to ensure that we were fitting only to the stellar and nebular continuum SED components. We used the Bruzual & Charlot ([2003]) models, and assumed a flexible dust attenuation law following Salim, Boquien & Lee ([2018]) and a double power-law star formation history with
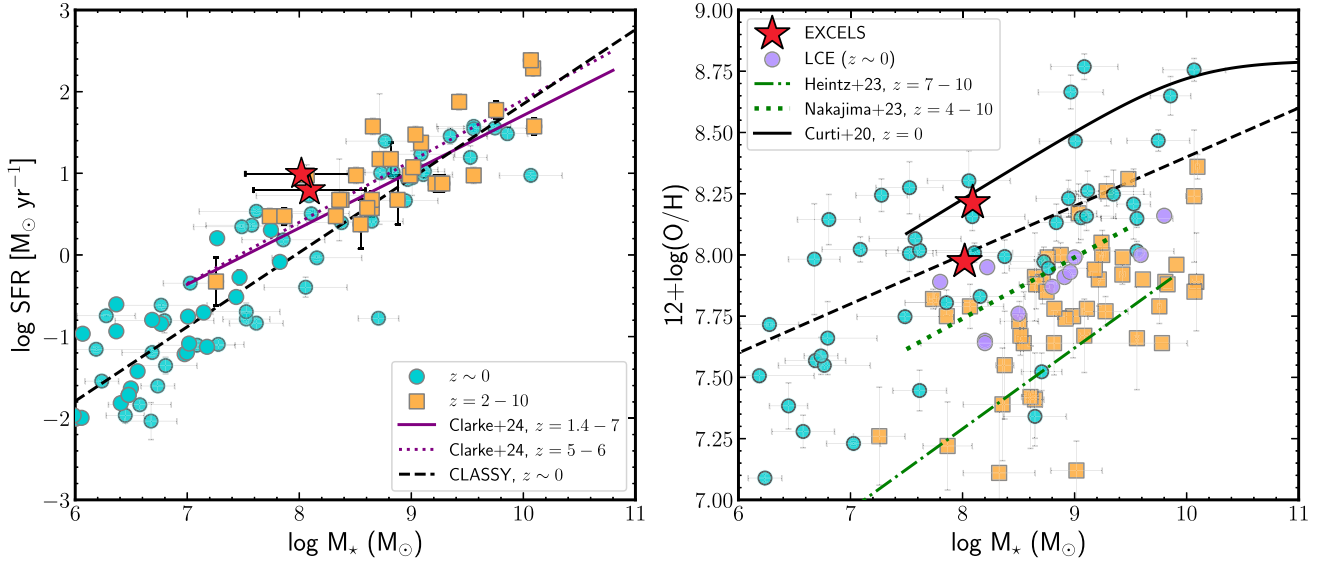
Figure 5. *Left:* the SFR versus stellar mass relation for the EXCELS galaxies at $z \simeq 5$ (red stars), along with an additional sample from the literature. SFGs at $z \simeq 0$ galaxies (circles) are taken from Berg et al. (2016), Berg et al. (2019a), Izotov et al. (2023), Ravindranath et al. (2020), Senchyna et al. (2022), Berg et al. (2022), and at $z > 2$ (squares) from Sanders et al. (2023b), Morishita et al. (2024), Marques-Chaves et al. (2024), Citro et al. (2024), Jones et al. (2023), Arellano-Córdova et al. (2024), Llerena et al. (2023), Schaerer et al. (2024), Isobe et al. (2023a), Rogers et al. (2024), Topping et al. (2024b, a), and Curti et al. (2025). The solid and dotted lines shows the SFR–$M_\star$ relation from Clarke et al. (2024) at $1.4 < z < 7$ and $5 < z < 6$, respectively. The dashed line shows the SFR–$M_\star$ relation for the CLASSY sample (Berg et al. 2022). The high-redshift galaxies and local analogues fall on the same SFR–$M_\star$ sequence despite the clear differences in metallicity. *Right*: the MZR for the same sample including LCE galaxies distinguished from other local SFGs for comparison purposes (Izotov et al. 2023; purple circles). The MZR for the CLASSY high-redshift analogue sample is shown as the dashed line (Berg et al. 2022), while the solid line represents the average MZR for all local SFGs Curti et al. (2020). In addition, two MZRs from high-redshift studies are indicated with dotted and dot–dashed lines from Nakajima et al. (2023) ($z = 4$–10) and Heintz et al. (2023) ($z = 4$–10), respectively. We find that the two EXCELS galaxies $z \simeq 5$ are metal-rich in comparison to other galaxies at similar redshifts, and are in fact consistent with the CLASSY MZR.

a Kroupa (2001) IMF; nebular continuum emission was included in the fitting but emission lines were excluded. Full details of the BAGPIPES fitting for the EXCELS star-forming sample are given in Scholte et al. (2025). The resulting stellar masses and SFRs are listed in Table 3. We derive stellar masses of $\log(M_\star/M_\odot) = 8.09^{+0.24}_{-0.15}$ and $\log(M_\star/M_\odot) = 8.02^{+0.06}_{-0.08}$ for EXCELS-70864 and EXCELS-121806, respectively. These stellar masses are similar those of other $z > 6$ galaxies (e.g. Curti et al. 2025; Hsiao et al. 2024; see also Sec 4.1). In addition to returning the best-fitting physical properties, these SED fits also returned an estimate of the stellar continuum SED which we used to correct the Balmer line fluxes for underlying stellar absorption (see Scholte et al. 2025). The Balmer absorption corrections were small for both EXCELS-70864 and EXCELS-121806 (< 2 per cent).

We also derived the SFR for both galaxies using the observed Hα fluxes (see Table 2). The luminosity distances for EXCELS-70864 and EXCELS-121806 were calculated based on the redshifts reported in Table 3 and used to convert the Hα fluxes to luminosities, $L(\text{H}\alpha)$. The SFR was estimated using the relation between SFR and $L(\text{H}\alpha)$ reported in Reddy et al. (2018) with a conversion factor of 3.236×10^{-42} erg s^{-1}, which is appropriated for low-metallicity systems. We derived values of $\log(\text{SFR}/M_\odot \text{yr}^{-1}) = 0.79 \pm 0.01$ for EXCELS-70864 and $\log(\text{SFR}/M_\odot \text{yr}^{-1}) = 1.00 \pm 0.01$ for EXCELS-121806. In both cases, we find excellent agreement between the SFR derived from the SED fitting and the Hα flux.

In the left-hand panel of Fig. 5 we show the position of the EXCELS galaxies in the star-forming main-sequence plane compared to the sample from the literature. The different lines correspond to the relations between SFR and stellar mass for galaxies at $z \sim 0$ from the CLASSY survey (Berg et al. 2022; dashed line) and galaxies

at a similar redshift (Clarke et al. 2024; dotted and solid lines). It can be seen that the two EXCELS galaxies agree well with the relation derived for the $z \sim 0$ CLASSY sample, the additional sample of galaxies at $z \geq 2$, and the relations from Clarke et al. (2024). Therefore, the global properties of the local and high-redshift samples are clearly comparable.

4 CHEMICAL ABUNDANCE PATTERNS

In this section, we first present the total metallicity (i.e. oxygen abundance) of our two $z \simeq 5$ galaxies before investigating the N/O and C/O ratios as a function of metallicity and stellar mass. Throughout we compare with our local and high-redshift comparison samples. Finally, we compare our results with bespoke chemical evolution models following the Kobayashi et al. (2020) prescription to explore the potential enrichment scenarios for our two galaxies.

4.1 The gas-phase oxygen abundance

In the left-hand panel of Fig. 5 we show the position of our two EXCELS galaxies in the mass–metallicity plane compared to our additional samples. The metallicities we derive are 12+log(O/H) $= 8.21^{+0.08}_{-0.05}$ for EXCELS-70864 and 12+log(O/H) $= 7.97^{+0.05}_{-0.04}$ EXCELS-121806 (i.e. $Z \simeq 0.3 Z_\odot$ and $Z \simeq 0.2 Z_\odot$, respectively.) As a result, both galaxies are in fact consistent with the mass–metallicity relation (MZR) derived for the local CLASSY sample at $z \simeq 0$ (Berg et al. 2022). At fixed stellar mass, they both have higher metallicities than the majority of the $z \geq 2$ SFGs in our comparison sample, and the local LCE from Izotov et al. (2023). Remarkably, the
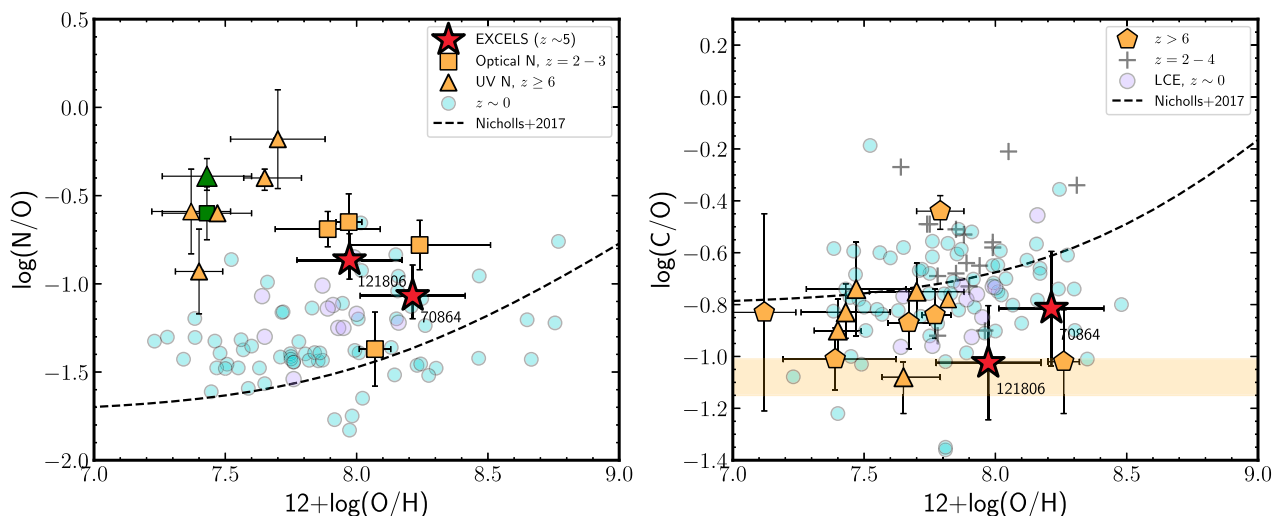
Figure 6. *Left-hand panel:* the N/O − O/H values for the EXCELS galaxies (red stars) compared with SFGs at different cosmic epochs. The circles represent galaxies at $z \simeq 0$ (Berg et al. 2016, 2019a, 2022 Ravindranath et al. 2020; Senchyna et al. 2022; Izotov et al. 2023, Arellano-Cordova et al. in preparation), while squares shows galaxies at $z = 2 − 3$ with N/O determined using optical lines from Sanders et al. (2023a) ($z \sim 2$), Rogers et al. (2024) (Q2343-D40; $z \sim 2.96$) and Welch et al. (2025) (Sunburst Arc; $z = 2.37$). SFGs with N/O determined using UV emission lines (N III] and/or [N IV]) are shown as triangles. LCE at $z \simeq 0$ from Izotov et al. (2023) are depicted by purple circles. Additionally, our N/O result using only optical lines from Topping et al. (2024b) for RXCJ2248-ID is included as a green triangle, while the UV N/O is shown as a green square. The EXCELS galaxies fall above the mean value of N/O for the local CLASSY sample and there appears to be a general trend whereby galaxies at $z > 2$ lie systematically above the local relation. *Right-hand panel:* a similar comparison in the C/O − O/H plane. Galaxies with both C and N abundances (i.e. that appear in both panels) are represented by triangles. We also include C/O measurements from Llerena et al. (2023) at at $z = 2 − 4$. The yellow shading represents the C/O ratio from pure CCSNe enrichment derived using chemical evolution models in Jones et al. (2023). The EXCELS galaxies have higher O/H compared the with other high-redshift galaxies but show consistent C/O ratios. In both panels the dashed line shows the relations reported in Nicholls et al. (2017) for N/O and C/O based on Milky Way stellar abundances.

metallicities are not far below the *average* $z = 0$ MZR from Curti et al. (2020).

In Fig. 5, we have also added the MZRs derived by Heintz et al. (2023) and Nakajima et al. (2023) for galaxies at $z = 7 − 10$ and $z = 4 − 10$, respectively, although we note that these MZRs are derived using strong-line calibrations to infer the metallicity. That being said, Morishita et al. (2024) have reported direct metallicity determinations for galaxies at $z \simeq 3 − 9$, which are consistent with the relation of Heintz et al. (2023). A comparison to these high-redshift relations makes it clear that EXCELS-70864 and EXCELS-121806 are both metal rich for their stellar mass at $z \simeq 5$, with metallicities that are directly comparable to local analogues from the CLASSY sample; these results again highlight the potentially large scatter in the metallicities of high-redshift galaxies that is only revealed using direct T_e-based metallicity constraints.

These relatively high metallicities offer the opportunity to place new unique constraints on CNO abundance patterns in high-redshift galaxies. As we discuss below, most galaxies at $z \gtrsim 5$ with direct C, N, and O abundance estimates have $12 + \log(O/H) \lesssim 7.8$; our observations will therefore place the first constraints on comparatively 'metal-rich' galaxies in the early Universe.

4.2 The N/O abundance ratio

In the left-hand panel of Fig. 6, we show the N/O abundance ratio of our two galaxies as a function of metallicity. It can be seen that, compared to the $z \simeq 0$ samples, both $z \simeq 5$ galaxies fall within the upper envelope of N/O at fixed O/H.[5] Therefore, in contrast to

some of the highly N-enriched galaxies that have been reported at $z > 6$ (e.g. Bunker et al. 2023; Marques-Chaves et al. 2024), the N enrichment of our sources is not unprecedented compared to what is observed locally. This difference might be explained by the fact that the metallicity of our sample is slightly larger than the typical metallicity of these notable N-rich galaxies (see Fig. 6). In fact, when compared to SFGs at slightly lower redshift ($z = 2 − 3$; orange squares) which have similar O/H, it can be seen that our N/O measurements are generally consistent within the uncertainties (Sanders et al. 2023a; Citro et al. 2024; Rogers et al. 2024; Welch et al. 2024).

However, despite the fact that some $z \simeq 0$ galaxies have similar N/O at fixed O/H, there does appear to be a general trend for the high-redshift galaxies to be more N-enriched than the typical local sources (Fig. 6). Of our two $z \simeq 5$ galaxies, EXCELS-121806 in particular is clearly more N-rich than the majority of the $z = 0$ sample. In general, if we consider all of the $z > 2$ sources, 12/14 (85 per cent) have $\log(N/O) > −1$ compared to only 8/58 (14 per cent) of the local samples. Of these local sources, it is clear that the LCEs of Izotov et al. (2023) have systematically higher N/O compared to the CLASSY sample, which Izotov et al. (2023) conclude is an indication of additional sources of N enrichment in these highly ionized galaxies. Still, the majority of $z > 2$ galaxies, including our two $z \simeq 5$ EXCELS sources, display a higher N/O than the typical $z = 0$ LCE.

---

[5]We also infer the N/O ratio using strong-line methods from Pérez-Montero & Contini (2009), Hayden-Pawson et al. (2022), and Florido, Zurita & Pérez-

Montero (2022). These methods are mainly based on samples of local SFGs and H II regions. For EXCELS-70864 and EXCELS-121806, we infer average values of $\log(N/O) = −1.13$ and $\log(N/O) = −1.02$, respectively. These values are 0.06 and 0.16 dex lower than those calculated using the T_e-sensitive method, but they are in agreement within the uncertainties.

If we compare directly to the $z \simeq 2 - 3$ galaxies with $12 + \log(\text{O/H}) \simeq 8.0$, to which our two EXCELS galaxies seem most comparable, there is evidence for a potentially large scatter in N/O in high-redshift galaxies. Sanders et al. (2023a) reported an elevated N/O ratio (using [N II] $\lambda 6584$) for two high specific SFR (sSFR) galaxies at $z \simeq 2$ (sSFR $\simeq 20\,\text{Gyr}^{-1}$) and attribute the N/O enhancement to the accretion of pristine gas which dilutes the overall metallicity content while preserving N/O. Similarly, Welch et al. (2025) recently reported the abundance patterns of different elements derived from a stacked spectrum of the Sunburst Arc galaxy at $z=$ 2.37, finding a N/O enrichment for this galaxy which they attribute to the possible signature enrichment of WR stars. On the other hand, Rogers et al. (2024) report the N/O ratio of a $z \simeq 3$ galaxy (Q2343-D40) that is in good agreement with the average N/O − O/H relation observed locally (see Fig. 6).

Overall, the comparison in the left panel of Fig. 6 suggests that the N/O ratios at fixed O/H of our $z \simeq 5$ galaxies are not unprecedented when compared to the local sample. Despite this, they do seem to follow a general trend in which galaxies at $z \gtrsim 2 - 3$ fall systematically above the average local N/O − O/H relation. This systematic offset suggests that the high-redshift population seems to be, on average, more N-rich than their local counterparts. More samples of direct-method N measurements at $z \gtrsim 5$ are needed to robustly demonstrate this claim.

4.3 Inferring N/O from UV emission lines

One potentially important difference between estimates of N/O above and below $z \simeq 6$ is the fact that, at $z > 6$, the abundances of N are determined primarily using UV emission lines as opposed to the optical [N II] $\lambda 6584$ line we have used. Indeed, the unexpected detection of the N III] $\lambda\lambda 1747$-1750 (quintuplet) or N IV $\lambda\lambda 1483,1486$ lines with *JWST* has opened a new pathways to the analysis of the different ionization states of N and their ionic and total abundances at $z > 6$ (e.g. Bunker et al. 2023; Cameron et al. 2023). Several studies have reported significant N/O enrichment in galaxies at $z > 6$ based on these lines (Bunker et al. 2023; Cameron et al. 2023; Curti et al. 2025; Senchyna et al. 2024; Marques-Chaves et al. 2024; Schaerer et al. 2024; Topping et al. 2024b, a; see Fig. 6). These results imply an additional enrichment to understand the high N/O in the early Universe (e.g. Charbonnel et al. 2023; Senchyna et al. 2024; Kobayashi & Ferrara 2024).

Topping et al. (2024b) presents an analysis of C and N in a lensed galaxy at $z = 6.1$ (RXCJ2248-ID). Interestingly, the spectrum of RXCJ2248-ID provides information on three different ionization states of N: [N II] in the optical and N III] and [N IV] in the UV. Topping et al. (2024b) derived the N/O abundance ratio using only the UV lines, resulting in a very high value of N/O (see Table 1). Since in Topping et al. (2024b) they do not report the N/O ratio using the optical [N II] line, we have used the [N II] $\lambda 6584$ flux listed in Topping et al. (2024b) to derive the abundance ratio of N/O following the same method applied to our $z \simeq 5$ sources (we report this value in Table 1). In Fig. 6, we show the two values of N/O derived using either the optical N lines (green square) or the UV N lines (green triangle) for RXCJ2248-ID. The optical-based N/O ratio (green square) is 0.21 dex lower than UV-based estimate, although consistent within the uncertainties. In addition, by taking advantage of the three different ionization states of N for RXCJ2248-ID, we also infer the N/O ratio without using an ICF assuming that N/O = (N$^+$ + N^{2+} + N^{3+})/(O$^+$ + O^{2+}). Therefore, we have calculated a value of $\log(\text{N/O}) = -0.52^{-0.18}_{+0.06}$, which is 0.08 dex higher than optical N/O reported in Table 1. This value is also consistent with the N/O

derived using $\log(\text{C}^{++}/\text{N}^{++}$ in combination with $\log(\text{C/O})$ present in Topping et al. (2024b) (see also Berg et al. 2018; Curti et al. 2025). Despite the slightly lower value, the optical N/O estimate remains extremely high at fixed O/H compared to local galaxies.

This comparison suggests that there is no significant bias in the N/O ratios in the optical and UV; the lower N/O of our sample compared to the $z > 6$ samples in Fig. 6 is likely not a result of the differences in the lines used to calculate the N abundance. However, this is only one example, and it should be kept in mind that the N/O ratio derived from UV lines might be sensitive to different ISM conditions (i.e. high-density gas; Pascale et al. 2023; Senchyna et al. 2024) that could, in principle, systematically bias UV and optical estimates. Larger samples of combined UV and optical N abundance measurements are needed to fully explore this issue.

4.4 The C/O abundance ratio

We now turn to the C abundances of our two $z \simeq 5$ galaxies. We have calculated $\log(\text{C/O}) = -0.82 \pm 0.22$ and $\log(\text{C/O}) = -1.02 \pm 0.22$ for EXCELS-70864 and EXCELS-121806 respectively. Using only the UV lines we reassuringly find a fully consistent value of $\log(\text{C/O}) = -1.07 \pm 0.43$ (see Table 3). In the right-hand panel of Fig. 6 we show the C/O versus O/H abundance ratios for the EXCELS galaxies compared to the additional literature samples. As in the left-hand panel, the local LCE are identified as purple circles to distinguish them from the local dwarf SFGs from CLASSY. Galaxies which have both C/O and N/O abundance estimates are shown as triangles; galaxies with only C/O measurements are identified with pentagons. It can be seen that, in contrast to N/O, the C/O ratios of the EXCELS galaxies – and the other high-redshift sources – fall systematically below the local SFGs.

Our two new measurements suggest these low C/O ratios extend to higher metallicities in agreement with the result of Citro et al. (2024), who analysed a lensed galaxy at $z = 3.77$ (J0332-3557) with a similar metallicity and find a similarly low C/O abundance. Citro et al. (2024) concluded that the low C/O is probably due to the enrichment of massive stars and low star formation efficiency.

These low C/O abundance ratios imply that the source of enrichment is likely a result of the rapid enrichment of massive stars or other exotic scenarios, for instance, very massive stars (e.g. Watanabe et al. 2024). This scenario would be consistent with the young ages derived from SED modelling (< 100 Myr) which would mean that enrichment of C via low-mass stars ($1 - 4\,\text{M}_\odot$; Henry et al. 2000; Kobayashi et al. 2020) has not had time to take place. The additional sample of galaxies at $z > 6$ shows similarly low C/O for metallicities in the range $12 + \log(\text{O/H}) = 7.12 - 7.70$ (e.g. Arellano-Córdova et al. 2022; Jones et al. 2023; Isobe et al. 2023b; Marques-Chaves et al. 2023; Topping et al. 2024b). At these low metallicities, there is better overlap between the high-redshift and local samples (see Fig. 6), suggesting a common source of C enrichment at the same time as a significant differences in N enrichment in these sources. At the higher metallicity of our sample, systematic offsets in both N/O and C/O seem to be present, although large sample sizes are clearly needed at $12 + \log(\text{O/H}) > 8$.

Focusing briefly on other literature analyses, Jones et al. (2023) measured $\log(\text{C/O}) = -1.01$ for GLASS−15008 ($z = 6.23$) and suggest that the C enrichment can be explained purely by massive-star CCSNe. Similarly, Curti et al. (2025) analysed the C/O enrichment of a galaxy at $z = 9.38$ using chemical evolution models, and again concluded that the C/O enrichment is consistent with the yields from massive-star CCSNe. On the other hand, Hsiao et al. (2024) recently
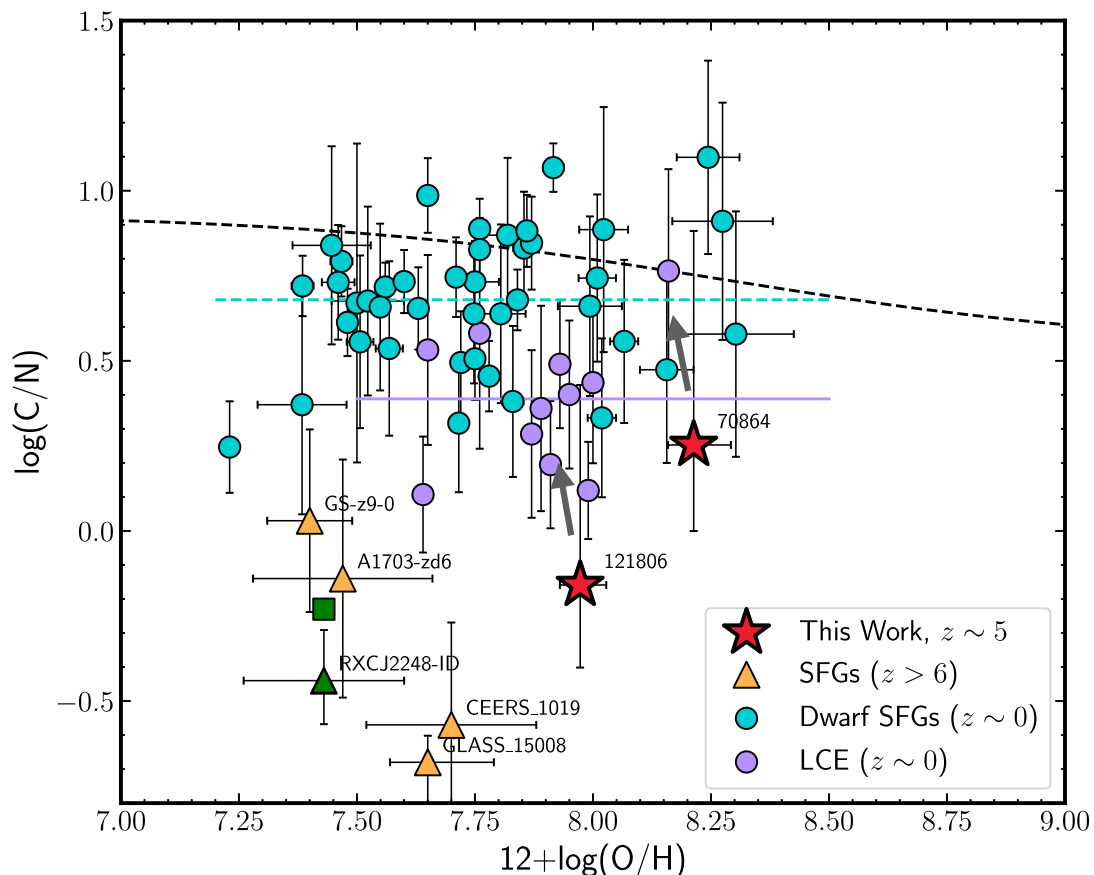
Figure 7. The C/N–O/H relationship for the EXCELS galaxies at $z \simeq 5$ compared to literature samples. The sample of local dwarf SFGs and LCEs are represented with circles (Berg et al. 2012, 2016; Izotov et al. 2023; Arellano-Córdova et al. in preparation; Martinez et al. in preparation). The blue dashed and purple solid lines show the mean of two local dwarf SFGs and LCEs, respectively. The triangles show the high-redshift galaxies from Isobe et al. (2023b) (GLASS_15008; $z = 6.23$), Marques-Chaves et al. (2024) (CEERS_1019; $z = 8.63$), Topping et al. (2024b) (RXCJ2248-ID; $z = 6.11$), Topping et al. (2025) (A1703-zd6; $z = 7.04$), Schaerer et al. (2024) (GN-z9p4, $z = 9.38$), and Curti et al. (2025) (GS-z9-0, $z = 9.43$). The C/N ratio that we have derived using the optical [N II] $\lambda6584$ line reported in Topping et al. (2024b, RXCJ2248-ID) is shown as the green square (see Section 4). The EXCELS galaxies and other high-redshift galaxies fall systematically below the average C/N ratios of the local analogues. The grey arrows indicate dust vector (the position of the EXCELS galaxies) for assuming small amounts of reddening indicated by the higher order Balmer line ratios (see Section 3). The dashed line represents the relation from Nicholls et al. (2017) based on Milky Way stellar abundances.

reported a high $\log(C/O) = -0.44^{+0.06}_{-0.07}$ for a galaxy at $z = 10.17$ (MACS0647-ID) at relatively low metallicity (see Table 1). These authors concluded that it might be associated with the enrichment of carbon from intermediate-mass stars that start to appear, given the age (> 100 Myr) implied in one of the clusters of MACS0647-ID.

Overall, it seems that the enrichment of C/O in our two EXCELS galaxies is most likely attributed to the yields of massive stars via CCSNe, before significant enrichment from low-mass AGB stars has begun to affect the ISM. The same explanation can also be used to explain the low C/O ratios observed across the majority of high-redshift sources (barring the Hsiao et al. 2024 measurement). Nevertheless, additional samples of galaxies at $z \simeq 5$ with T_e measurements are clearly still required to fully assesses O/H variations and improve our understanding of C production at early times.

4.5 The cosmic evolution of C/N

Bringing the abundances of C, N, and O together offers further insights into the star formation time-scales and enrichment pathways in SFGs (e.g. Henry et al. 2000; Berg et al. 2019a). For example, at low metallicities (i.e. after the onset of star formation), a plateau is

expected based on the C and N yields of the most massive stars; this should be subsequently followed by deviations due to N-enrichment from intermediate-mass stars, then C-enrichment from low-mass stars (e.g. Peña-Guerrero et al. 2017; Berg et al. 2019a; Kobayashi et al. 2020; Izotov et al. 2023).

In Fig. 7, we show the C/N – O/H relation for our two EXCELS galaxies compared to the additional sample (where measurements of both C and N are available). In this element abundance ratio diagram, the different enrichment pathways of the high-redshift and local samples are clearly evident. Broadly, there appears to be a separation between the local and high-redshift samples at $\log(C/N) \simeq 0$. We find that 100 per cent of the local sample fall above this value, compared to only 1/8 (EXCELS-70864; $\simeq 10$ per cent) of the high-redshift sample. As was evident from Fig. 6, the high-redshift galaxies appear to be preferentially enriched in N compared to C; our two new measurements hint that this trend may extend to more metal-rich systems than have previously been observed.

In general, as can also be seen from Fig. 6, we find that our $z \simeq 5$ galaxies display C/N ratios that are closer to the local LCE than to the local CLASSY high-redshift analogue sample. We find values of $\langle \log(C/N) \rangle = 0.69 \pm 0.21$ for the local high-redshift-analogues

(consistent with the mean value derived in Berg et al. 2019a) and $\langle \log(C/N) \rangle = 0.38 \pm 0.20$ for the local LCE (both indicated by horizontal lines in Fig. 7). Both of our $z \simeq 5$ measurements fall below these average values, although much closer to the LCE. Although it is not the focus of this work, we note that this kind of abundance ratio comparison between local LCE and high-redshift galaxies might offer an alternative pathway to understanding the escape fraction of ionizing photons during the reionization epoch.

At this point, it is worth highlighting the most important systematic uncertainty in our results, namely the effect of dust reddening. In Fig. 7 we have indicated with arrows the shift in the C/N and O/H abundances when adding relatively modest amounts of reddening ($E(B - V) = 0.15$). We have used the extinction law of Cardelli, Clayton & Mathis (1989, $R_V = 3.1$)[6] for dust correction. It can be seen that the shift in C/N is potentially significant, while O/H remains similar; this large C/N shift is a result of the large wavelength separation between the C and N emission lines ($\Delta\lambda_{\rm rest} \simeq 4500$ Å). Crucially, any dust reddening moves the high-redshift samples closer to the local samples. Despite the relatively high metallicity of our $z \simeq 5$ galaxies, we consider our estimate of $E(B - V) = 0$ to be robust; moreover, we note that some of the CLASSY galaxies with similar metallicity also display zero/negligible reddening. Nevertheless, it is important to emphasize that deep spectra with accurate nebular reddening corrections are crucial for this kind of CNO abundance analysis.

4.5.1 Chemical evolution models

In order to gain a deeper understanding of the possible chemical enrichment pathways of these two EXCELS galaxies, we have constructed illustrative chemical evolution models following the prescriptions of Kobayashi et al. (2020) and Kobayashi & Ferrara (2024) including WR stars. Our aim is to use these models to help us understand the O/H versus C/N relation shown in Fig. 7, but we emphasize that we are not attempting to find an exact match to the star formation and chemical abundance history (doing so would be infeasible given the large uncertainties).

We consider a standard IMF with a slope of $x = 1.3$ in the mass range $0.01\,M_\odot \leq M \leq 120\,M_\odot$ (equation 2 Kroupa 2001). In addition, we investigate the use of a shallow (i.e. more top-heavy) and steep (i.e. more bottom-heavy) IMF by considering slopes of $\alpha - 1 = x = 1.1$, $x = 1.9$, and $x = 2.3$. We consider a toy star formation history that we consider plausible for $z = 5$ galaxies and that yields the correct oxygen abundance at the redshift of our sources. The star formation history consists of an early rising phase followed by a strong burst $\simeq 1$ Gyr after the onset of star formation in which the SFR increases by $\simeq 2$ orders of magnitude. The assumed star formation history for each of the IMFs is illustrated in Fig. 8. For a shallower IMF, a larger mass-loss from massive stars makes the star formation history slightly extended (the ejected material provides additional fuel for star formation). As we use the same star formation and infall time-scales for these models (3 Gyr for the initial star formation, 0.1 Gyr for the second star burst), the increase of stellar feedback for a shallower, more top-heavy, IMF is not accounted for here.

Figure 8. Chemical evolution models illustrating the affect of different IMFs on the C/N abundance ratios. *Top panel:* a set of representative star formation histories assuming a shallow IMF ($x = 1.1$; black dashed line), a Kroupa (2001) IMF ($x = 1.3$; red solid line), and a steeper IMF ($x = 1.9$ and $x = 2.3$; dot–dashed and dotted lines, respectively). For reference, the teal dashed line shows the redshift of the EXCELS galaxies. *Bottom panel:* the evolution of the C/N ratio with respect to metallicity, compared with observations the EXCELS observations. The chemical evolution models are generated based on the prescriptions of Kobayashi et al. (2020) and Kobayashi & Ferrara (2024). The different lines indicate the IMF slope used in each model. For reference, the cyan and purple lines indicate the mean value of C/N for local SFGs and LCE as in Fig. 7. The chemical evolution models assuming bottom-heavy IMF are a better match to the C/N ratios of the EXCELS galaxies, although the uncertainties are clearly significant and a standard IMF is not ruled out.

In the bottom panel of Fig. 8, we show the resulting chemical enrichment pathways in the O/H versus C/N plane and compare with our EXCELS observations. For reference, we have also indicated the mean values of C/N for the dwarf SFGs and LCE samples. The characteristic up-and-down 'U-shaped' model curves can be understood by considering the relative enrichment time-scales of C and N. After the onset of the second star formation episode, a galaxy will be rapidly enriched in O (increasing O/H[7] and decreasing (C,N)/O ratios) followed by N enrichment from intermediate-mass AGB stars ($M_\odot \simeq 4$–$7\,M_\odot$) that will cause a decrease in C/N (and

---

[6]As an additional inspection, we explore the impact of adopting the Small Magellanic Clouds extinction law by Gordon et al. (2003) on our results of the C/N ratios (see Fig. 7). We find that the resulting C/N ratios differ by 0.10–0.12 dex, which represents a shift of comparable magnitude to that obtained when using the extinction law of Cardelli et al. (1989).

[7]The small decrease of O/H is caused by dilution with the gas infall that triggers the second star burst.

increase N/O ratio). Eventually, low-mass AGB stars ($\simeq 1$–$4\,M_\odot$) will begin to enrich the ISM with C after $t \simeq 1.3$ Gyr, which is not shown in this figure. As can be seen in Fig. 8, for a steeper IMF galaxies will reach a lower value of C/N before C-enrichment from low-mass stars kicks in. The reason for this is because, for a steeper IMF, there are a greater proportion of N-enriching $M_\odot \simeq 4$–$7\,M_\odot$ stars relative to the massive stars $M_\odot \gtrsim 10\,M_\odot$ that provide the initial C-enrichment.

It can be seen that the standard IMF model is able to reproduce the mean values of C/N for the local samples (cyan and purple lines). Although this standard IMF model is also formally consistent with EXCELS-70864 and EXCELS-121806 within the uncertainties, it falls systematically above both observed C/N ratios. Instead, we find that the steeper IMF models seem to align better with the C/N ratios observed in the EXCELS galaxies. Taken at face value, this comparison suggests that, if anything, a steeper IMF provides a better explanation for the observed low C/N ratios in metal-enhanced, evolved systems at $z \simeq 5$.

This is different from what is found for the metal-poor galaxy at $z \simeq 9$ presented in Curti et al. (2025). For that galaxy, the observed CNO abundances were explained by a single star burst (with much shorter time-scales: $\tau_s = 0.0002$, $\tau_i = 0.001$ Gyr), and a top-heavy IMF for PopIII ($x = 0$ for $30 - 120\,M_\odot$) was preferred. Our galaxy is 0.6 dex more metal-rich, and we find that it is not possible to explain the observed CNO abundances with a single star burst in this case. For more evolved metal-rich systems extended star formation histories are needed to account for the build-up in overall metallicity, and because of this AGB enrichment from intermediate-mass stars ($M_\odot \simeq 4$–$7\,M_\odot$) also needs to be considered. The simultaneous need to a top- and bottom-heavy to explain C/N ratios at $z > 5$ across a wide range of metallicities might be achieved using, for example, a concordance IMF (e.g. van Dokkum & Conroy 2024).

However, for now the comparison is purely illustrative. Much larger samples of C and N measurements and more sophisticated modelling (i.e. complex star formation histories, the inclusion of stellar feedback mechanisms) are clearly needed before any firm conclusion can be drawn. Nevertheless, these models demonstrate that, contrary to metal-poor systems, low C/N ratios in more metal-rich systems are less likely to be a result of a top-heavy IMF.

5 SUMMARY AND CONCLUSIONS

We have presented a study of the physical properties and chemical composition of two galaxies at $z \simeq 5$ from the *JWST*-EXCELS survey (Carnall et al. 2024). Both galaxies benefit from medium-resolution (R = 1000) *JWST*/NIRSpec spectroscopy covering their rest-frame UV to optical spectra across the wavelength range $\lambda_{\rm rest} \simeq 1600$–$8000$ Å. This wide rest-frame wavelength coverage enables the measurement of several key nebular emission lines. Crucially, via the detection of the faint [O III] $\lambda 4363$ auroral line in both objects, we have derived robust chemical abundance estimates for several elements. In this paper, we have focused in particular on the C/O and N/O abundance ratios, which are accessible due to the detection of the UV C III] $\lambda 1909$ and optical [N II] $\lambda 6584$ features. We have compiled a literature sample of SFGs at $z \simeq 0$ up to $z \simeq 10$ with which we can compare our results. Crucially, there are currently only four other examples of galaxies at $z \gtrsim 5$ with direct estimates of C, N, and O. Our measurements therefore significantly expands upon the current sample. Finally, we have interpreted our measured abundance ratios using the chemical evolution models of Kobayashi et al. (2020). Our main results can be summarized as follows:

(i) Both galaxies are relatively metal-rich for their stellar mass (Fig. 5). For EXCELS-70864 we estimate $\log(M_\star/M_\odot) = 8.09^{+0.24}_{-0.15}$ and $12 + \log({\rm O/H}) = 8.21^{+0.08}_{-0.05}$ ($Z \simeq 0.3\,Z_\odot$) and for EXCELS-121806 we estimate $\log(M_\star/M_\odot) = 8.02^{+0.06}_{-0.08}$ and $12 + \log({\rm O/H}) = 7.97^{+0.05}_{-0.04}$ ($Z \simeq 0.2\,Z_\odot$). Interestingly, both galaxies appear to lie within the high-metallicity tail of the $z \gtrsim 4$ MZR and are fully consistent with the average MZR measured for the local ($z \simeq 0$) high-redshift analogue sample from the CLASSY survey (Fig. 5).

(ii) We measure H α-based SFRs of 6.2 ± 0.1 and $10 \pm 0.2\,M_\odot\,{\rm yr}^{-1}$ for EXCELS-70864 and EXCELS-121806, respectively, meaning that both galaxies are consistent with the $M_\star$–SFR sequence formed from the local analogue and high-redshift ancillary samples (Fig. 5). We therefore find a striking similarity between our two $z \simeq 5$ galaxies and local dwarf SFGs from CLASSY in terms of their global physical properties, namely stellar mass, SFR, and total metallicity.

(iii) However, a detailed inspection of their chemical abundance patterns reveals some differences. Focusing first on the N/O abundance ratio, we find that EXCELS-70864 and EXCELS-121806 fall within the high-N/O tail of the local distribution (Fig. 6). Unlike other notably extreme examples of high N/O at $z \gtrsim 6$ in the literature (e.g. Bunker et al. 2023; Topping et al. 2024b) the N/O values we measure can be found among local systems and are therefore not unprecedented. However, our measurements continue a trend in which the majority of direct N/O measurements at $z \gtrsim 5$ fall systematically above the average local N/O–O/H relation, with $\log({\rm N/O}) \gtrsim -1.0$ (Fig. 6). These results might suggest that, even at higher metallicities, a source of N-enrichment exists that is common in the early Universe is absent in typical local dwarf SFGs.

(iv) In contrast to the relatively high N/O ratios, we find that the C/O ratios are low and fall below the local C/O–O/H relation (Fig. 6). In general, we find that the C/O ratios we measure are consistent with other $z \gtrsim 5$ galaxies in the literature, which all fall close to the pure CCSNe yield expectation of $\log({\rm C/O}) \simeq -1.1$. These results suggest the C is enriched mainly by CCSNe at these high redshifts, without significant input from low-mass AGB stars (Kobayashi et al. 2020).

(v) Combing the C, N, and O abundances in the C/N versus O/H plane reveals a separation between the local and high-redshift galaxies (Fig. 6). While all local galaxies lie at $\log({\rm C/N}) > 0$, the vast majority of high-redshift systems fall below this threshold. Again, these results suggest a preferential enrichment of N over C in the ISM of galaxies at $z \gtrsim 5$. Our new results suggest that the excess in N relative to C might also extend to moderately enriched galaxies ($Z \simeq 0.2$–$0.3\,Z_\odot$; Fig. 6).

(vi) To gain further insight into the chemical abundance ratios of our $z \simeq 5$ galaxies, we explore a variety of scenarios using the chemical evolution models of Kobayashi et al. (2020). We model the star formation histories as steadily rising followed by a recent burst that elevates the SFR to $\simeq 10\,M_\odot\,{\rm yr}^{-1}$. In general, we find that models with steeper IMF slopes (i.e. a bottom-heavy IMF) do a better job at explaining the observed abundance ratios (Fig. 8). The fundamental reason for this is that a steeper, more bottom-heavy IMF provides more intermediate-mass AGB stars ($M_\odot \simeq 4$–$7\,M_\odot$) to enrich the ISM with primary production of N. However, given the uncertainties, our analysis is also fully consistent with standard IMF models. Ultimately, more data are needed to draw robust conclusions, but our models demonstrate that, contrary to the most metal-poor systems (e.g. Curti et al. 2025), a more top-heavy IMF is likely not favoured as an explanation for low C/N ratios in moderately enriched high-redshift galaxies.

Our analysis shows that deep *JWST* data can provide robust direct-method chemical abundance ratios for SFGs at $z \simeq 5$. We find that the preferential enrichment of N seen in low-metallicity galaxies at high redshift might also extend to more moderate metallicities ($Z \simeq 0.2$–$0.3\,Z_\odot$). Contrary to the top-heavy IMF invoked to explain low C/N ratios in metal-poor high-redshift galaxies, a comparison with chemical evolution models suggests that, if anything, a steeper bottom-heavy IMF is favoured by our data. However, the current sample sizes remain small, and more data are needed to any draw firm conclusions. Thankfully, the wavelength coverage of NIRSpec means that similar studies can be carried out across the redshift range $4 < z < 7$; dedicated programs should therefore be capable of significantly increasing sample sizes of galaxies with direct C, N, and O abundances.

ACKNOWLEDGEMENTS

DATA AVAILABILITY

All data will be shared by the corresponding author upon reasonable request.

REFERENCES

Allen M. G., Groves B. A., Dopita M. A., Sutherland R. S., Kewley L. J., 2008, ApJS, 178, 20

Amorín R. O., Pérez-Montero E., Vílchez J. M., 2010, ApJ, 715, L128

Arellano-Córdova K. Z., Rodríguez M., 2020, MNRAS, 497, 672

Arellano-Córdova K. Z. et al., 2022, ApJ, 940, L23

Arellano-Córdova K. Z. et al., 2024, ApJ, 968, 98

Asplund M., Amarsi A. M., Grevesse N., 2021, A&A, 653, A141

Astropy Collaboration, 2018, AJ, 156, 123

Astropy Collaboration, 2022, ApJ, 935, 167

Baldwin J. A., Phillips M. M., Terlevich R., 1981, PASP, 93, 5

Bekki K., Tsujimoto T., 2023, MNRAS, 526, L26

Berg D. A. et al., 2012, ApJ, 754, 98

Berg D. A., Skillman E. D., Henry R. B. C., Erb D. K., Carigi L., 2016, ApJ, 827, 126

Berg D. A., Erb D. K., Auger M. W., Pettini M., Brammer G. B., 2018, ApJ, 859, 164

Berg D. A., Erb D. K., Henry R. B. C., Skillman E. D., McQuinn K. B. W., 2019a, ApJ, 874, 93

Berg D. A., Chisholm J., Erb D. K., Pogge R., Henry A., Olivier G.M., 2019b, ApJ, 878, L3

Berg D. A., Chisholm J., Erb D. K., Skillman E. D., Pogge R. W., Olivier G. M., 2021, ApJ, 922, 170

Berg D. A. et al., 2022, ApJS, 261, 31

Berrington K. A., Burke P. G., Dufton P. L., Kingston A. E., 1985, At. Data Nucl. Data Tables, 33, 195

Bertin E., Arnouts S., 1996, A&AS, 117, 393

Bruzual G., Charlot S., 2003, MNRAS, 344, 1000

Bunker A. J. et al., 2023, A&A, 677, A88

Cameron A. J., Katz H., Rey M. P., Saxena A., 2023, MNRAS, 523, 3516

Cardelli J. A., Clayton G. C., Mathis J. S., 1989, ApJ, 345, 245

Carnall A. C., McLure R. J., Dunlop J. S., Davé R., 2018, MNRAS, 480, 4379

Carnall A. C., Leja J., Johnson B. D., McLure R. J., Dunlop J. S., Conroy C., 2019, ApJ, 873, 44

Carnall A. C. et al., 2024, MNRAS, 534, 325

Castellano M. et al., 2024, ApJ, 972, 143

Charbonnel C., Schaerer D., Prantzos N., Ramírez-Galeano L., Fragos T., Kuruvanthodi A., Marques-Chaves R., Gieles M., 2023, A&A, 673, L7

Citro A., Berg D. A., Erb D. K., Auger M. W., Becker G. D., James B. L., Skillman E. D., 2024, ApJ, 969, 148

Clarke L., Shapley A. E., Sanders R. L., Topping M. W., Brammer G. B., Bento T., Reddy N. A., Kehoe E., 2024, ApJ, 977, 133

Croxall K. V., Pogge R. W., Berg D. A., Skillman E. D., Moustakas J., 2016, ApJ, 830, 4

Cullen F. et al., 2019, MNRAS, 487, 2038

Cullen F. et al., 2021, MNRAS, 505, 903

Curti M., Mannucci F., Cresci G., Maiolino R., 2020, MNRAS, 491, 944

Curti M. et al., 2025, A&A,697, 24,

D'Eugenio F. et al., 2024, A&A, 689, A152

De Robertis M. M., Dufour R. J., Hunt R. W., 1987, J. R. Astron. Soc. Can., 81, 195

Dors O. L. et al., 2013, MNRAS, 432, 2512

Esteban C., García-Rojas J., Peimbert M., Peimbert A., Ruiz M. T., Rodríguez M., Carigi L., 2005, ApJ, 618, L95

Florido E., Zurita A., Pérez-Montero E., 2022, MNRAS, 513, 2006

Flury S. R. et al., 2022, ApJS, 260, 1

Flury S. R., Arellano-Córdova K. Z., Moran E. C., Einsig A., 2024, preprint (arXiv:2412.06763)

Garnett D. R., 1990, ApJ, 363, 142

Garnett D. R., 1992, AJ, 103, 1330

Glass R., 1983, Ap&SS, 92, 307

Gordon K. D., Clayton G. C., Misselt K. A., Landolt A. U., Wolff M. J., 2003, ApJ, 594, 279

Hayden-Pawson C. et al., 2022, MNRAS, 512, 2867

Heintz K. E. et al., 2023, A&A, 679, A91

Henry R. B. C., Edmunds M. G., Köppen J., 2000, ApJ, 541, 660

Horne K., 1986, PASP, 98, 609

Hsiao T. Y.-Y. et al., 2024, preprint (arXiv:2409.04625)

Hu W. et al., 2024, ApJ, 971, 21

Hunter J. D., 2007, Comput. Sci. Eng., 9, 90

Isobe Y., Ouchi M., Nakajima K., Harikane Y., Ono Y., Xu Y., Zhang Y., Umeda H., 2023a, ApJ, 956, 139

Isobe Y. et al., 2023b, ApJ, 959, 100

Izotov Y. I., Stasińska G., Meynet G., Guseva N. G., Thuan T. X., 2006, A&A, 448, 955

Izotov Y. I., Schaerer D., Worseck G., Berg D., Chisholm J., Ravindranath S., Thuan T. X., 2023, MNRAS, 522, 1228

James B. L. et al., 2022, ApJS, 262, 37

Ji X. et al., 2024, MNRAS, 535, 881

Jones T. et al., 2023, ApJ, 951, L17

Kauffmann G. et al., 2003, MNRAS, 346, 1055

Kennicutt R. C. Jr, Bresolin F., Garnett D. R., 2003, ApJ, 591, 801

Kewley L. J., Dopita M. A., Sutherland R. S., Heisler C. A., Trevena J., 2001, ApJ, 556, 121

Kewley L. J., Jansen R. A., Geller M. J., 2005, PASP, 117, 227

Kluyver T. et al., 2016, in Loizides F., Schmidt B., eds, IOS Press, Positioning and Power in Academic Publishing: Players, Agents and Agendas. p. 87–90

Kobayashi C., Ferrara A., 2024, ApJ, 962, L6

Kobayashi C., Karakas A. I., Umeda H., 2011, MNRAS, 414, 3231

Kobayashi C., Karakas A. I., Lugaro M., 2020, ApJ, 900, 179

Kroupa P., 2001, MNRAS, 322, 231

Llerena M. et al., 2023, A&A, 676, A53

Luridiana V., Morisset C., Shaw R. A., 2015, A&A, 573, A42

Maiolino R. et al., 2024, Nature, 627, 59

Marques-Chaves R. et al., 2024, A&A, 681, A30

McClymont W. et al., 2024, MNRAS, 540, 190

Mingozzi M. et al., 2022, ApJ, 939, 110

Mingozzi M. et al., 2024, ApJ, 962, 95

Morishita T. et al., 2024, ApJ, 971, 43

Moustakas J., Buhler J., Scholte D., Dey B., Khederlarian A., 2023, Astrophysics Source Code Library, record ascl:2308.005

Nakajima K., Ouchi M., Isobe Y., Harikane Y., Zhang Y., Ono Y., Umeda H., Oguri M., 2023, ApJS, 269, 33

Nicholls D. C., Sutherland R. S., Dopita M. A., Kewley L. J., Groves B. A., 2017, MNRAS, 466, 4403

Nussbaumer H., Storey P. J., 1978, A&A, 64, 139

Osterbrock D. E., 1989, Astrophysics of Gaseous Nebulae and Active Galactic Nuclei. University Science Books, Mill Valley, CA.

Osterbrock D. E., Ferland G. J., 2006, Astrophysics of Gaseous Nebulae and Active Galactic Nuclei. University Science Books, Mill Valley, CA.

Pascale M., Dai L., McKee C. F., Tsang B. T. H., 2023, ApJ, 957, 77

Peimbert M., Costero R., 1969, Boletin de los Observatorios Tonantzintla y Tacubaya, 5, 3

Peimbert M., Peimbert A., Delgado-Inglada G., 2017, PASP, 129, 082001

Peña-Guerrero M. A., Leitherer C., de Mink S., Wofford A., Kewley L., 2017, ApJ, 847, 107

Pérez-Montero E., Contini T., 2009, MNRAS, 398, 949

Pérez-Montero E., Hägele G. F., Contini T., Díaz Á. I., 2007, MNRAS, 381, 125

Ravindranath S., Monroe T., Jaskot A., Ferguson H. C., Tumlinson J., 2020, ApJ, 896, 170

Reddy N. A. et al., 2018, ApJ, 869, 92

Rivera-Thorsen T. E. et al., 2024, A&A, 690, A269

Rogers N. S. J., Skillman E. D., Pogge R. W., Berg D. A., Moustakas J., Croxall K. V., Sun J., 2021, ApJ, 915, 21

Rogers N. S. J., Strom A. L., Rudie G. C., Trainor R. F., Raptis M., von Raesfeld C., 2024, ApJ, 964, L12

Salim S., Boquien M., Lee J. C., 2018, ApJ, 859, 11

Sanders R. L. et al., 2023a, ApJ, 943, 75

Sanders R. L., Shapley A. E., Topping M. W., Reddy N. A., Brammer G. B., 2023b, ApJ, 955, 54

Sanders R. L., Shapley A. E., Topping M. W., Reddy N. A., Brammer G. B., 2024, ApJ, 962, 24

Scarlata C., Hayes M., Panagia N., Mehta V., Haardt F., Bagley M., 2024, preprint (arXiv:2404.09015)

Schaerer D., Marques-Chaves R., Xiao M., Korber D., 2024, A&A, 687, L11

Scholte D. et al., 2025, MNRAS 540 1800

Senchyna P. et al., 2022, ApJ, 930, 105

Senchyna P., Plat A., Stark D. P., Rudie G. C., Berg D., Charlot S., James B. L., Mingozzi M., 2024, ApJ, 966, 92

Shapley A. E. et al., 2015, ApJ, 801, 88

Shapley A. E. et al. 2025 ApJ 980, 242

Skillman E. D., Berg D. A., Pogge R. W., Moustakas J., Rogers N. S. J., Croxall K. V., 2020, ApJ, 894, 138

Stanton T. M. et al., 2024, MNRAS, 532, 3102

Stanton T. M. et al., 2025, MNRAS, 537, 1735

Stasińska G., 1982, A&AS, 48, 299

Steidel C. C. et al., 2014, ApJ, 795, 165

Steidel C. C., Strom A. L., Pettini M., Rudie G. C., Reddy N. A., Trainor R. F., 2016, ApJ, 826, 159

Topping M. W., Shapley A. E., Reddy N. A., Sanders R. L., Coil A. L., Kriek M., Mobasher B., Siana B., 2020, MNRAS, 495, 4430

Topping M. W. et al., 2025, ApJ 980, 225

Topping M. W. et al., 2024b, MNRAS, 529, 3301

van der Walt S., Colbert S. C., Varoquaux G., 2011, Comput. Sci. Eng., 13, 22

van Dokkum P., Conroy C., 2024, ApJ, 973, L32

Vincenzo F., Belfiore F., Maiolino R., Matteucci F., Ventura P., 2016, MNRAS, 458, 3466

Vink J. S., 2023, A&A, 679, L9

Virtanen P. et al., 2020, Nat. Methods, 17, 261

Watanabe K. et al., 2024, ApJ, 962, 50

Welch B. et al., 2025, ApJ, 980, 33

Wiese W. L., Fuhr J. R., Deters T. M., 1996, J. Phys. Chem. Ref. Data Monogr., 7, 403

Yan Z., Jerabkova T., Kroupa P., 2017, A&A, 607, A126

Yanagisawa H. et al., 2024, ApJ, 974, 180

This paper has been typeset from a TₑX/LᴬTₑX file prepared by the author.